

Revision 2

1 **Textural and mineral chemical evidence for the cumulate origin and evolution of high-**  
2 **titanium basalt fragment 71597**

3 Patrick H. Donohue<sup>1\*</sup> and Clive R. Neal<sup>1</sup>

4 <sup>1</sup>Civil and Environmental Engineering and Geological Sciences, University of Notre Dame,  
5 Notre Dame, IN 46556, U.S.A.

6 \*Corresponding author: [phd2@alumni.nd.edu](mailto:phd2@alumni.nd.edu); Present Address: Hawai'i Institute of Geophysics  
7 and Planetology, University of Hawai'i at Manoa, 1680 East-West Road, POST 602, Honolulu,  
8 HI 96822 USA.

9 **Abstract**

10 Basalt fragment 71597 is the sole high-titanium mare basalt showing evidence for olivine  
11 accumulation during formation. The petrogenesis of this unique sample was investigated using  
12 quantitative textural analysis and major- and trace-element mineral geochemistry. Crystal size  
13 distribution analysis identified two size populations of olivine, which we separate into cumulate  
14 and matrix olivine. The spatial distribution of olivine also supports clustering of olivine crystals,  
15 likely during accumulation. Observed mineral chemistry was consistent with an origin through  
16 olivine accumulation, although where this occurred cannot be discerned (e.g., in ponded melts at  
17 the base of or in the lunar crust, or within a thick high-Ti basalt flow). Attempts to place 71597  
18 within a geochemical group were inconclusive both using subtraction of cumulate olivine from  
19 bulk composition, and by modal recombination of major phases. However, equilibrium liquid  
20 compositions of augite and plagioclase are determined to be consistent with an origin by  
21 fractionation from the Type B2 chemical suite of Apollo 17 high-Ti basalts. This method of  
22 classification has potential for placing other Type U (“Unclassified”) basalts into chemical  
23 suites.

Revision 2

24

25 **Keywords:** *mare basalts, cumulates, crystal size distributions, LA-ICP-MS*

26

27

## 28 **Introduction**

29 Olivine cumulates have been recovered from multiple lunar locales, although they form  
30 only a small part of the mare basalt sample collection. The majority of cumulates are low-  
31 titanium ( $\text{TiO}_2 < 6 \text{ wt.}\%$ ) composition comprising Apollo 12 ilmenite basalts 12005 and 12036  
32 (Dungan and Brown 1977; Rhodes et al. 1977), several members of the Apollo 12 olivine basalt  
33 suite (Neal et al. 1994), Apollo 15 basalts 15385 and 15387 (Ryder 1985), Apollo 14 clast  
34 14305,122 (Taylor et al. 1983), and six fragments in lunar meteorite NWA 773 (Jolliff et al.  
35 2003). The only high-Ti cumulate is basalt 71597 (8.4 wt%  $\text{TiO}_2$ ), a 12.35 g fragment collected  
36 with Apollo 17 mission rake samples (Murali et al. 1977; Warner et al. 1977). The composition  
37 and formation of this fragment relative to Apollo 17 high-Ti basalts provides information on an  
38 end-member of lunar volcanic textures.

39 Whole-rock analyses (major and trace element abundances) conducted by neutron  
40 activation techniques (Murali et al. 1977) and mineral compositions (major element) have been  
41 interpreted to indicate basalt 71597 experienced 24-27% olivine and possible minor ilmenite  
42 accumulation (Warner et al. 1977). The evidence for accumulation described by Warner et al.  
43 (1977) can be summarized in four main points:

- 44 • 71597 contains the highest whole-rock MgO content (15.8 wt%) and the highest modal  
45 olivine abundance (19.3%) of any high-Ti basalt.

Revision 2

- 46 • Whole-rock REE abundances are lower than – but sub-parallel to – typical Apollo 17 high-  
47 Ti basalts, indicating dilution by REE-poor olivine ( $\pm$  ilmenite).
- 48 • There is a bimodal distribution of olivine Fo-content between large, anhedral olivine cores  
49 and small “matrix” olivine grains (Figure 1).
- 50 • It is unusual to find olivine crystals several millimeters in size in a coarse-grained matrix,  
51 as large olivine crystals within other Apollo 17 samples are typically found as phenocrysts  
52 in fine-grained basalts (*e.g.*, 74275).

53 Warner et al. (1979) further suggested 71597 originated in a Type B flow (after Rhodes et  
54 al. 1976; separated into Type B1 and B2 by Neal et al. 1990). However, the small sample size of  
55 71597 (12.35 g; Neal and Taylor 1993) and coarse grain size has precluded the determination of  
56 an incontrovertibly representative whole-rock analysis, which means that 71597 remains  
57 unclassified. Apollo 17 high-Ti basalts are classified into several groups (Types A, B1, B2, C, D,  
58 and U for “unclassified”) on the basis of whole-rock geochemistry (Rhodes et al. 1976; Warner  
59 et al. 1979; Neal et al. 1990; Ryder 1990). Type A basalts contain 50-60% higher incompatible  
60 trace element abundances than the other groups (Rhodes et al. 1976). Types B1 and B2 basalts  
61 were split primarily on the basis of La/Sm ratios (Neal et al. 1990). Type C basalts contain high  
62 MgO and Cr<sub>2</sub>O<sub>3</sub>, and have less ilmenite on the liquidus at early stages of crystallization. The  
63 Type D group is defined by a single basalt fragment (,2144) from drive tube 79001, and has the  
64 highest MgO/TiO<sub>2</sub> ratio and lowest incompatible trace element abundance of any other classified  
65 Apollo 17 basalt (Ryder 1990). Classification schemes for Apollo 17 basalts are weighted toward  
66 incompatible elements, and are thus strongly affected by the amount of mesostasis and late stage  
67 components sampled. This effect is more pronounced in samples where <1 g material is used in

Revision 2

68 bulk analyses (e.g., Haskin and Korotev 1977). Thus, the bulk composition of 71597 determined  
69 using a 0.61 g subsample (Murali et al. 1977) still may not be representative.

70 The explanation for the origin of 71597 given by Warner et al. (1977) favors the  
71 formation of large, skeletal olivine and ilmenite crystals towards the margins of a large flow that  
72 accumulate via gravitational settling towards the flow's interior. Other processes, such as mixing  
73 of magmas containing different crystal cargoes, have not been explored. Aspects of mare  
74 volcanic processes and the nature of olivine accumulation (e.g., gravitational settling during a  
75 single, large flow versus magma mixing) can be addressed by mineral geochemistry and  
76 quantitative petrographic analysis. We present electron probe microanalysis and laser ablation  
77 inductively couple plasma mass spectrometry (LA-ICP-MS) analyses of mineral phases in two  
78 new thin sections of basalt 71597. Microscale details of basalt evolution are recorded in core-to-  
79 rim and inter-crystal compositional variations, and can best be constrained by *in-situ* techniques.  
80 In addition, equilibrium liquid trace element compositions are used to constrain a petrogenetic  
81 model of magma evolution. We also undertake quantitative petrography on 71597 through  
82 Crystal Size Distribution (CSDs; Marsh 1988, 1998; Cashman and Marsh 1988; Higgins 2000,  
83 2002, 2006; Higgins and Roberge 2003) and Spatial Distribution Patterns (SDPs; Jerram et al.  
84 2003) analysis. Particularly relevant to this study is the work of Day and Taylor (2007) who  
85 demonstrated that a combined CSD-SDP approach could show not only variability in cooling  
86 rates, but also the importance of clumping and formation of clustered crystal frameworks during  
87 the cooling of lunar lava flows. Additional studies have demonstrated the practicality of using  
88 the CSD technique to differentiate endogenous mare basalts from impact melts (Cushing et al.  
89 1999; Neal et al. 2015), and the CSD-SDP methods to equate Apollo 17 samples with  
90 experimentally determined cooling rates (Donohue and Neal 2015).

91

## Samples and Methodology

92

As noted above, the coarse grain size and small mass of 71597 has precluded an

93

unambiguously representative whole-rock analysis. This represents an issue of obtaining

94

representative CSD-SDP analyses of the sample due to its coarse grain size. In order to alleviate

95

the effect of non-representivity when undertaking a textural analysis of 71597, two thin sections

96

were requisitioned from sub-sample 71597,0, designated 71597,12 and 71597,13 (Figure 1). The

97

data obtained from each thin section were combined where possible, allowing for a more robust

98

statistical analysis.

99

### Crystal Size Distribution (CSD) and Spatial Distribution Profile (SDP) Methods

100

The application of CSD and SDP methods to lunar basalts has been discussed in detail in

101

Day and Taylor (2007) and Donohue and Neal (2015). We present a brief summary here.

102

Quantitative textural analyses were conducted on digital photomicrograph mosaics (Figure 1).

103

Crystal outlines were manually traced in the *Adobe Photoshop*© program using reflected light

104

photomosaics for ilmenite, and plane polarized light photomosaics for olivine, pyroxene, and

105

plagioclase. Crystals larger than ~0.03 mm could be traced at the image resolution; smaller

106

crystals were not included in the analyses due to issues with resolution and intersection effects,

107

where grains smaller than the thin section thickness are underrepresented. Monomineralic layers

108

were processed in the image-processing program *ImageJ* (ver. 1.44m) (Schneider et al. 2012) to

109

determine crystal center coordinates (X,Y), major and minor crystal axis lengths and areas. Best-

110

fit 3D crystal dimensions were estimated from a database of major and minor axis lengths,

111

*CSDSlice* (Morgan and Jerram 2006). Stereological corrections were made using the

112

*CSDCorrections* (ver. 1.3.9) program (Higgins 2000) to calculate a semi-logarithmic CSD of

113

population density versus size. Crystal populations were split into size bins with five bins per

Revision 2

114 decade (each size bin contains a range of crystal lengths 0.2 times larger than the previous).  
115 Using more than five bins per decade introduces errors because there are fewer crystals in each  
116 bin, and because more cycles of correction are needed during stereological conversion (Higgins  
117 2000).

118 A reliable estimate of 3D crystal shape requires at least 75 total crystals (for tabular  
119 morphologies); a minimum of 250 crystals is recommended for more acicular shapes (Morgan  
120 and Jerram 2006). A size bin must contain three or more crystals in order to calculate upper and  
121 lower uncertainties on the population density. The *CSDCorrections* program calculates a  
122 goodness of fit ( $Q$ ) of the data to a straight line, which allows for quantitative distinction  
123 between linear ( $Q > 0.1$ ), sub-linear ( $Q$  between 0.001 and 0.1) and non-linear ( $Q < 0.001$ ) CSDs  
124 (Higgins 2006). Sub-populations can also be isolated if a CSD appears kinked rather than curved.  
125 A CSD is considered kinked if the profile can be divided into two (or more) linear segments with  
126 unique slopes.

127 The CSD profile slope is a function of crystallization and is the inverse reciprocal of a  
128 characteristic crystal length ( $C_L$ ) for a given population (Marsh 1988). The  $C_L$  is the product of  
129 growth rate ( $G$ ) multiplied by residence time ( $\tau$ ). Growth rate is typically approximated based on  
130 experimental work and for a given phase may vary by several orders of magnitude between and  
131 even within specific studies (e.g., Burkhard 2005; Cabane et al. 2005; Vinet and Higgins 2010).  
132 For example, it is evident that temperature plays a critical role in growth rate (e.g., Burkhard  
133 2005), which changes throughout crystallization. Thus, without additional knowledge of the  
134 system from which a phase crystallized, there are significant assumptions associated with  
135 residence time calculations and, therefore, potentially significant errors are introduced.  
136 Therefore, we do not use calculated absolute residence times as part of this study.

137           The mineral SDPs can be used to investigate the relative ordering and frameworks of  
138 mineral phases. Relative ordering is quantified by “*R*” values, where *R* is determined by  
139 comparing observed phase distributions to a similarly-sized population of randomly packed  
140 spheres (Jerram et al. 1996, 2003). *R* can be compared to the percent matrix (porosity) to  
141 distinguish touching from non-touching frameworks, as well as the relative ordering or clustering  
142 of phases. The SDP is a function of spatial relationships, and because we do not know exactly  
143 the separation of the two thin sections, the SDP is calculated for individual thin sections.  
144 Combining CSD and SDP analyses allows the effects of crystal nucleation and growth, magma  
145 mixing (Martin et al. 2006), and the relative position of a given sample in lava flows and  
146 intrusions (Jerram et al. 2003, 2010; Day and Taylor 2007; Donohue and Neal 2015).

#### 147 **Major and trace element analysis**

148           Major element compositions of select ilmenite, pyroxene, plagioclase, and olivine  
149 crystals were obtained using a JEOL JXA-8200 electron microprobe at the Earth and Planetary  
150 Sciences Microanalysis Facility, Washington University in St. Louis (St. Louis, MO). The  
151 microprobe was equipped with five wavelength-dispersive spectrometers and a JEOL (e2v /  
152 Gresham) silicon-drift energy-dispersive spectrometer. Beam operating conditions were 15 kV  
153 accelerating potential, 25 nA probe current, and a 5 micrometer spot size. A defocused beam  
154 (~10 micrometers diameter) was used to avoid loss of volatiles (e.g., Na, K) during plagioclase  
155 analyses.

156           Compositional analyses of several large (>10  $\mu\text{m}$ ) melt inclusions in olivine and ilmenite  
157 crystals, as well as additional olivine (spot and line raster), armalcolite, and mesostasis analyses  
158 were obtained using a Cameca SX50 electron microprobe at the University of Chicago (Chicago,  
159 IL; see Supplementary Table S1). Line raster analyses were obtained across two large, partially

Revision 2

160 resorbed olivines in 71597,12. Typical operating conditions were 15 kV accelerating potential  
161 and a 30 nA probe current and a 1 or 5 micrometer spot size (for oxides and silicates,  
162 respectively).

163 Trace element abundances of crystals were obtained using an Element2 inductively  
164 coupled plasma mass spectrometer (ICP-MS) coupled to a UP213 Nd:YAG laser ablation system  
165 at the Notre Dame Midwest Isotope and Trace Element Research Analytical Center (MITERAC,  
166 Notre Dame, IN). Laser operating conditions were 5 Hz repetition rate and 5 ns pulse duration to  
167 achieve  $<15 \text{ J/cm}^2$  fluence for 15-80  $\mu\text{m}$  beam sizes. An optimum carrier gas (He) flow rate of  
168  $0.6 \text{ L min}^{-1}$  was used to move ablated particles downstream to a 'Y'-connection where it was  
169 mixed with Ar-gas and introduced to the mass spectrometer. The NIST SRM 610 (for olivine,  
170 ilmenite, and armalcolite) and NIST SRM 612 (for plagioclase and pyroxene) glasses (Pearce et  
171 al. 1997) were used for external calibration purposes. Detection limits ( $3\sigma$ ) for pyroxene  
172 calculated in GLITTER<sup>®</sup> (van Achterberg et al. 2001) were 0.001-0.03 ppm for Y, Nb, Cs, La,  
173 Ce, Pr, Nd, Sm, Eu, Tb, Dy, Ho, Er, Tm, Lu, Hf, Ta, Th, U; 0.03-1 ppm for Sc, Mn, Co, Ga, Rb,  
174 Zr, Ba, Gd, Yb, Pb; 1-5 ppm for Cr, Ni, Sr; 5-10 ppm for Ti; and  $>200$  ppm for Ca. Detection  
175 limits for plagioclase were 0.03-1 ppm for Y, Sm, Eu, Dy, and Er, and similar to that for  
176 pyroxene for other elements. Analyses of ilmenite and olivine were performed in medium  
177 resolution (resolution = mass/peak width of  $\sim 4000$ ) to reduce spectral interferences, but at the  
178 cost of reduced sensitivity. Thus, detection limits for elements in olivine and Fe-Ti oxides were  
179 0.08-5 ppm for Sc, V, Co, Y, Zr, Sr, Hf, Ta; 5-20 ppm for Cr and Mn; 20-100 ppm for Ti and Ni  
180 in olivine; and 100-200 ppm for Ti in Fe-Ti oxides. The Ti-content obtained by microprobe was  
181 utilized as the internal standard for ilmenite and armalcolite; similarly, MnO was the internal  
182 standard for olivine, and CaO for plagioclase and pyroxene. Data were reduced using the



Revision 2

183 GLITTER<sup>®</sup> software, which allows for time-resolved background (~50 seconds) and signal (~60  
184 seconds) selection. Cracks, inclusions and adjacent phases were avoided using a combination of  
185 transmitted and reflected light prior to ablation and confirmed by time-resolved signal review.

## 186 **Results**

### 187 **Textural Analysis**

188 In general, the two new thin sections are petrographically similar to the detailed  
189 description given by Warner et al. (1977), although absolute mineral abundances differ. Manual  
190 point-counting of 71597,12 (3,454 points over an area 67 mm<sup>2</sup>) shows the sample contains 37%  
191 pyroxene, 33% olivine, 15% plagioclase, and 15% opaques (ilmenite and trace armalcolite,  
192 spinel, and troilite). Warner et al. (1977) conducted point-counting over a larger area (~240  
193 mm<sup>2</sup>), and report less olivine (19.3%), more plagioclase (28.3%), and other minor differences  
194 compared point-counting results for 71597,12. Visual estimates of bulk fragments 71597,0 and  
195 71597,5 range from 19-30% olivine (Warner et al. 1977; Neal and Taylor 1993).

196 Olivine CSD profiles for 71597,12 and ,13 were previously presented in Neal et al.  
197 (2015). They are nearly identical and are multiply kinked, but the two largest size bins of the  
198 71597,12 olivine CSD do not contain statistically significant numbers of crystals (n=2 each)  
199 (Table 1, Figure 2a). In addition, only 43 olivine crystals could be reliably traced in 71597,13,  
200 almost half the recommended minimum for CSD calculations (Morgan and Jerram 2006). A  
201 more robust CSD was created by combining the olivine populations (n = 161) of 71597,12 and  
202 ,13. The resulting CSD (Figure 2a) is consistent with the individual sample CSDs with kinks at  
203 crystal lengths of ~0.4 mm and ~2.2 mm. However, the two largest size bins have the largest  
204 error and do not represent a statistically unique population, especially given the low number of  
205 crystals (n = 4) so we do not interpret this portion of the CSD as being a third distinct population

Revision 2

206 of olivine crystals. Consideration of all crystals  $>0.4$  mm in length yields a sub-linear CSD  
207 profile ( $Q = 0.013$ ) with a  $C_L$  of 0.57 mm. To avoid over-interpretation of the CSD data, we only  
208 consider the olivine CSD as representing two populations ( $C_L$  of 0.07 mm and 0.57 mm) in  
209 further calculations.

210 Ilmenite CSD profiles of both thin sections are indistinguishable, and strongly concave  
211 upward ( $Q \ll 0.001$ ) (Table 1, Figure 2b). Linear regression through the steep and shallow  
212 segments of the ilmenite CSD profile yields slopes corresponding to characteristic lengths of 0.4  
213 and 0.8 mm, respectively. The largest ilmenites (up to 1.1 mm as measured in thin section) are  
214 similar in habit to but not as large as the elongate skeletal ilmenite (up to 5 mm) reported by  
215 Warner et al. (1977). The CSD reconstructs 3D morphologies from 2D cross-sections. So, given  
216 the X:Y:Z shape ratios calculated for ilmenite, the “true” length of a randomly-oriented prismatic  
217 grain would likely be larger than the observed length. In addition, the CSD breaks population  
218 density (number of crystals for the measured area) into a range of sizes. The points represent the  
219 largest size of crystals in each bin, such that the 6.4 mm bin represents the population of crystals  
220 of sizes ranging from  $\sim 4$  to 6.4 mm. Therefore, the large crystal sizes observed by Warner et al.  
221 (1977) are represented in the analysis here.

222 Pyroxene and plagioclase CSDs for 71597,12 are sub-linear with  $Q$  of 0.001 and 0.01,  
223 respectively (Table 1, Figure 2c-d). The characteristic lengths range from 0.3-0.4 mm. There is  
224 also a downturn of the CSD profile at the smallest crystal sizes for pyroxene and plagioclase, a  
225 feature not observed in ilmenite or olivine CSDs. Pyroxene and plagioclase crystals extend to  
226 size bins below the estimated limit of resolution of the CSD technique, and so this downturn  
227 likely is due to an under-representation of these smaller crystal sizes.

Revision 2

228 Spatial distribution profiles were determined for pyroxene (porosity,  $P = 64\%$ ,  $R = 1.03$ ),  
229 plagioclase ( $P = 89\%$ ,  $R = 0.91$ ), ilmenite ( $P = 94\%$ ,  $R = 0.76$ ), and olivine ( $P = 90\%$ ,  $R = 0.59$ )  
230 in thin section 71597,12 (Table 1). Multiple thin sections cannot be combined for SDPs, as can  
231 be done for CSDs, because the SDP calculation is based on nearest neighbor distances. These  
232 SDP results are presented in Figure 3 along with SDP results of several Apollo 17 high-Ti basalts  
233 (Donohue and Neal 2015). Olivine and pyroxene form a touching crystal framework in 71597  
234 (Figure 3). The higher abundance of olivine appears to have offset the ilmenite and plagioclase  
235 populations to higher densities compared to other high-Ti basalts. A similar relationship was  
236 observed in low-Ti basalts (Day and Taylor 2007).

### 237 **Petrography and Mineral Chemistry**

238 Representative analyses of silicate, Fe-Ti oxide, and melt inclusion compositions are  
239 presented in Table 2 and Table 3 (all analyses are available in Supplementary Table S1). Large  
240 olivine crystals ( $Fo_{72-75}$ ) typically exhibit normal zonation to higher-Fe margins ( $Fo_{66-72}$ ) (Figure  
241 4). However, this zonation is less gradual at sharp olivine-olivine contacts or where mantled by  
242 titanite. Mantled olivines have a thin ( $<0.05$  mm) reaction rim. The cores of large olivine  
243 crystals are compositionally distinct from cores of small olivine crystals ( $Fo_{62-68}$ ). The data  
244 follow a crystal fractionation trend, wherein there is a corresponding decrease in Fo-content with  
245 decreasing Cr (698-1880 ppm) and V (17-55 ppm), and increasing Y (1.5-7.1 ppm) (Figure 5).  
246 Compared to olivine from other mare basalt suites as well as olivine vitrophyres, 71597 olivines  
247 have unique compositions in terms of Ti/V and Cr/Y ratios on plots of Ti/V and Cr/V against Fo  
248 contents (Figure 6).

249 Individual ilmenite compositions ( $n = 15$ ) are homogeneous in regards to major element  
250 abundance, with the range in Mg# (12-19) representing inter-crystal variation (Figure 7). Warner

Revision 2

251 et al. (1977) noted a broader range in ilmenite Mg# of 4-29 (MgO = 1-8 wt%) from an  
252 unreported number of crystals. Paired core and rim trace element analyses are also similar, with  
253 the exception of Co in one crystal in 71597,12 and Cr and Co in one crystal of 71597,13. In both  
254 cases, ilmenite rims show elevated Co abundance. There is inter-crystal variation, with a positive  
255 correlation between Zr (~110 to 750 ppm) and Hf (~5 to 20 ppm) (Figure 7). Ilmenite typically  
256 contains blebs and lamellae of rutile and Al-rich chromite (too small for analysis by LA-ICP-  
257 MS), with inclusions of silicate melt, troilite, and/or Fe-metal.

258 The sole armalcolite crystal observed is partially rimmed by an ilmenite grain of average  
259 composition. The armalcolite crystal itself is at the low MgO (5.6 wt%) and high Al<sub>2</sub>O<sub>3</sub> (2.0  
260 wt%) range of armalcolite compositions in Apollo 17 mare basalts (Dymek et al. 1975; Papike et  
261 al. 1974; Warner et al. 1975; Warner et al. 1976a). Stanin and Taylor (1980) experimentally  
262 constrained the relationship between the Fe/Ti<sup>3+</sup> component and oxygen fugacity in armalcolite.  
263 Our calculation of the Ti<sup>3+</sup> component yielded an average oxygen fugacity, relative to the iron-  
264 wüstite (IW) buffer, of IW-0.66 ± 0.2. This is within the range determined for high-Ti basalts  
265 collected during the Apollo 17 mission, where armalcolite *f*O<sub>2</sub> was found to range from IW-0.4  
266 to IW-0.8 (Stanin and Taylor 1980).

267 Pyroxene compositional variability is similar to that observed in Apollo 17 plagioclase-  
268 poikilitic mare basalts (Figure 8, Table 3). Titanaugite is present as discrete crystals and as  
269 mantles (up to 0.3 mm) on olivine. Pigeonite is limited to extreme margins of augite and small  
270 crystals near the margins of partially resorbed olivine. There is only minor Fe-enrichment (up to  
271 Fs<sub>35</sub>) in the crystals investigated here, although Warner et al. (1977) found ~5 pyroxenes with up  
272 to Fs<sub>50</sub>. The Al/Ti ratio decreases from 2.4:1 in augite to ~2:1 in augite rims and pigeonite  
273 crystals, and the absolute abundance of Al<sub>2</sub>O<sub>3</sub> and TiO<sub>2</sub> also decreases from core to rim in

Revision 2

274 individual crystals. Augite REE profiles are subparallel and convex upward with strong negative  
275 Eu anomalies ( $\text{Eu}/\text{Eu}^*$ , where  $\text{Eu}^* = \sqrt{[\text{Sm}_{\text{CN}} * \text{Gd}_{\text{CN}}]}$ , “CN” = CI Chondrite Normalized”) (Figure 8). Pigeonite and augite crystals are LREE depleted and have steep profiles from La-Sm,  
276 and relatively flat HREE profile. The La-Sm slope decreases with increasing total LREE  
277 abundance.

279 Plagioclase exhibits minor core-to-rim compositional zonation from  $\text{An}_{90}$  to  $\text{An}_{84}$  (Figure  
280 4). Poikilitic plagioclase grains contain 250-660 ppm Sr and 13-95 ppm Ba. One small grain  
281 (~0.2 mm;  $\text{An}_{84}$ ) in a partially resorbed olivine grain contains 1100 ppm Sr and 250 ppm Ba.  
282 REE profiles are typical for lunar basalts, with large positive Eu-anomalies of 42 to 83. The  
283 LREE profiles are flat, and inter-crystal REE-abundance varies by an order of magnitude (Figure  
284 8).

285 Silicate melt inclusions are common in large, partially resorbed olivine crystals (>20 melt  
286 inclusions in some olivines) and are ubiquitous in ilmenite laths. These melt inclusions generally  
287 range in size from <0.01 mm to 0.05 mm. The majority of melt inclusions in olivine are  
288 microcrystalline intergrowths of pyroxene and plagioclase, with occasional anhedral troilite or  
289 ilmenite. Melt inclusions in ilmenite are generally glassy and occasionally contain troilite.  
290 Compositions were determined by microprobe only (Supplementary Table S1) as the inclusion  
291 size precluded trace element determinations by LA-ICP-MS. There was some degree of host  
292 control on melt inclusion composition, where one melt inclusion in ilmenite contained lower  
293  $\text{TiO}_2$  compared to those in olivine and spinel, and one inclusion in spinel contained higher  $\text{Cr}_2\text{O}_3$   
294 than others. The largest melt inclusion (0.08 mm) was heterogeneous, with two separate analyses  
295 of 6.5 (center) and 4.5 (rim) wt% MgO. We did not have access to a heated stage to  
296 rehomogenize these inclusions but this remains as an avenue for future study.

297

## Discussion

### 298 Evidence of crystal accumulation

299 Using the methodology of Longhi et al. (1978) to calculate the equilibrium olivine  
300 composition for a given bulk composition, the Fe/Mg partition coefficient between melt and  
301 olivine was adjusted for TiO<sub>2</sub> content (Delano 1980). The equilibrium olivine composition  
302 calculated for 71597 using the bulk composition from Murali et al. (1977) is Fo<sub>83</sub>, which is not  
303 observed in this sample (Warner et al. 1977; this work). This suggests the bulk composition is  
304 not representative of a liquid composition as the MgO abundance is inflated due to olivine  
305 accumulation.

306 Jerram et al. (2003) have used SDP textural analysis to define crystal frameworks that  
307 have high melt porosity and are loosely packed (produced from a mixed population of irregular-  
308 shaped clusters or clumps of crystals), and more tightly packed frameworks with lower melt  
309 porosity (produced from individual crystals). Figure 3 evaluates 71597 petrography in terms of *R*  
310 and porosity, comparing the mineral data to those from other Apollo 17 high-Ti basalts  
311 (Donohue and Neal 2015). Pyroxene is the most abundant groundmass phase in the Apollo 17  
312 high-Ti basalts (e.g., Dymek et al. 1975; Neal et al. 1990) so it is not surprising that pyroxene  
313 from all Apollo 17 basalts, including 71597, create a touching framework of crystals (Figure 3).  
314 In comparison, the plagioclase analysis closest to the touching framework line ( $P = \sim 75\%$ ,  $R =$   
315 1.1) is from the equilibrated basalt 75015,52, which has the highest abundance of plagioclase (25  
316 vol%) of the Apollo 17 basalts reported by Donohue and Neal (2015). Relative to other Apollo  
317 17 basalts, plagioclase in 75015 has a lower calculated porosity (Figure 3), consistent with  
318 compaction or overgrowth (e.g., Jerram et al. 1996, 2003). Olivine in 71597,12 has the lowest *R*  
319 (0.59) of any phase, and is the sole non-pyroxene phase to create a touching crystal framework

Revision 2

320 (Figure 3). Compared to other high-Ti basalt olivine, the 71597 olivine SDP is offset to a lower  
321  $R$  and decreased porosity. This is an indication of increased poor sorting (i.e. accumulation), an  
322 interpretation further supported by the kinked olivine CSD reflecting two olivine crystal size  
323 populations (Fig. 2a). The combination of SDP and CSD analyses support the observation that  
324 olivine accumulation occurred as clusters in 71597 but was not a significant factor in any other  
325 high-Ti basalt (*cf.*, Neal et al. 1990; Donohue and Neal 2015).

326         Crystal size distribution characteristics (CSD profile slope, y-intercept, and linearity)  
327 vary between phases (Figure 2). However, direct comparisons first require accounting for  
328 variable growth rates of the different phases in order to estimate residence time of the different  
329 crystal cargoes present in 71597. It was noted above that growth rates are variable and are  
330 dependent on many factors that change as a magma crystallizes, which leads to residence times  
331 with large errors. We can, however, estimate relative residence times simply by examining the  
332 gradients of the CSD profiles. For olivine and ilmenite, the CSDs are divided into two segments.  
333 Warner et al. (1977) suggested there was some ilmenite accumulation in 71597, and here the  
334 CSD has been subdivided at ~1 mm size bin. The populations of larger olivine and ilmenite  
335 crystals have the lowest CSD gradients ( $-2.8 \pm 0.3$  and  $-1.5 \pm 0.1$ , respectively), indicating  
336 relatively longer residence times relative to other phases in 71597. This is consistent with the  
337 either prolonged olivine and ilmenite crystallization or accumulation of these phases.

338         The variation in modal olivine between our analysis and that of Warner et al. (1977) and  
339 Neal and Taylor (1993) indicates heterogeneous distribution of olivine at the thin section scale,  
340 consistent with crystal accumulation, possibly as clusters of olivine. The bimodal Fo-content  
341 distribution between large and matrix olivine (Figure 5) is also consistent with accumulation in  
342 an evolving melt. Furthermore, compositional data suggest accumulation from a fractionating

Revision 2

343 magma rather than from different magma batches, as there is no evidence of an antecryst origin  
344 for some olivines or for mixing between magmas with olivine on the liquidus. Olivine  
345 compositions also suggest that ilmenite was co-crystallizing with those containing the highest Fo  
346 contents, but ceased crystallizing around Fo<sub>69</sub> (Figure 6a).

347         The crystallization sequence and conditions for 71597 derived from textural analysis are  
348 consistent with sample geochemistry. The general sequence of crystallization is olivine +  
349 armalcolite → olivine + ilmenite → ilmenite + augite → ilmenite + augite + plagioclase →  
350 pigeonite + plagioclase. The CSDs and general textures indicate olivine crystallized first at an  
351 initial cooling rate of 1-3 degrees per hour (cf. Usselman et al. 1975; Usselman and Lofgren  
352 1976; Donohue and Neal 2015). Olivine and ilmenite were on the liquidus prior to eruption, and  
353 some matrix olivines likely crystallized at the surface. Ilmenite contains relatively high MgO  
354 contents (3.2-5.2 wt% MgO here, up to 8 wt% noted by Warner et al. 1977) compared to other  
355 Apollo 17 high-Ti basalts (0.17-4.87 wt% MgO), which may have resulted from reaction with  
356 the evolving melt during crystallization. This reaction is supported by abundant exsolution  
357 lamellae similar to those found in other re-equilibrated ilmenite from Apollo 17 basalts (e.g., El  
358 Goresy and Ramdohr 1975). This relatively high-Mg content in ilmenite is likely buffered by  
359 olivine resorption, with titanaugite and high-Ca plagioclase crystallization lowering CaO in the  
360 residual melt (as evidenced by decreasing CaO content in plagioclase with decreasing compatible  
361 element abundance) and leading to late pigeonite crystallization. There may also be a  
362 contribution from isothermal diffusion, which can inhibit Fe-enrichment commonly observed  
363 during pyroxene crystallization (e.g., Dungan and Brown 1977).

364 **Type source of 71597**



365 Mineral compositions and CSDs can be used to evaluate not only crystallization history  
366 but also source characteristics (e.g., Hui et al. 2011). Apollo 17 basalt 71597 is currently  
367 unclassified (being part of the “Type U” classification of Rhodes et al. 1976) because of the  
368 coarse grain size and small sample mass (12.35 g; Neal and Taylor 1993) making a  
369 representative whole-rock analysis difficult to produce. This is why the whole rock data reported  
370 by Murali et al. (1977) cannot be used to classify 71597. According to Haskin and Korotev  
371 (1977), Haskin et al. (1977), and Ryder and Schuraytz (2001), coarse grained samples require up  
372 to 5 grams of sample to be powdered in order to obtain a representative WR analysis. This would  
373 require consuming almost half of the original 12.35 g that comprised 71597. Murali et al. (1977)  
374 only used 0.612 g of this coarse-grained sample in their whole rock analysis, strongly suggesting  
375 this is not representative of the true whole rock composition. The data obtained as part of this  
376 study are used to propose a method for classifying 71597 within the chemical schemes already  
377 proposed, thus enhancing the science return on these precious samples.

378 Apollo 17 high-Ti basalts are separated into groups (Types A, B1, B2, C, D) based on  
379 whole-rock major and trace element abundances and ratios (Figure 9; Rhodes et al. 1976; Neal et  
380 al. 1990; Ryder 1990). For example, the Type B basalt suite first identified by Rhodes et al.  
381 (1976), and later split into Types B1 and B2, were divided based on whole rock rare earth  
382 element (REE) and high field strength element (HFSE) abundances and La/Sm ratios (Neal et al.  
383 1990). Prior to the split, Warner et al. (1979) proposed 71597 originated in a thick high-Ti basalt  
384 flow of Apollo 17 Type B basalt composition. The fraction of olivine in the bulk analysis has  
385 consequences for La, Sm, and Yb, which are controlled by the amount of mesostasis in the  
386 analysis (Haskin and Korotev 1977). However, ratios of these olivine-incompatible elements  
387 should be unaffected by olivine addition. Olivine ( $\pm$  ilmenite) accumulation should only dilute -

Revision 2

388 and not fractionate – elements incompatible in olivine (and ilmenite - e.g., REEs). We attempted  
389 to distinguish the Apollo 17 high-Ti basalt source group for 71597 by accounting for trace  
390 element variation caused by olivine accumulation. The reported La/Yb ratio (0.63; Murali et al.  
391 1977; Warner et al. 1977) is similar to Type B1 basalts, while the La/Sm ratio (0.77) is consistent  
392 with Type B2 basalts (Figure 9b,c). The Yb/Sm ratio (1.23) is higher than all other A17 high-Ti  
393 basalts (0.83-1.13). Uncertainty in the INAA-determined REE abundances reported by Murali et  
394 al. (1977) are given only in general terms of  $\pm 1-5\%$ . With this consideration, the Yb/Sm ratio of  
395 71597 may then be within uncertainty of the upper limit of Type B1 basalts. However, calculated  
396 pre-cumulate values for 71597 yield compositions outside any Apollo 17 group (Figure 9b),  
397 Type B2 basalts (Figure 9c), and Type B1 basalts (Figure 9d). The conflicting groupings and  
398 unique ratios of 71597 indicate at least some incompatible element ratios are not representative  
399 of the whole-rock.

400 Major element oxide compositions of Apollo 17 high-Ti basalts group into trends (Figure  
401 9) that can be explained by simple fractional crystallization evolution (*cf.* Neal et al. 1990).  
402 Warner et al. (1977) showed that subtraction of 24-27% olivine from the measured 71597 bulk  
403 composition brought the sample into the range of other high-Ti basalts (*cf.*, Table 4 of Warner et  
404 al. 1977). We expanded this model to include trace elements via Rayleigh fractionation.  
405 Incompatible trace element fractionation results (Table 4 and Figure 9) for removal of 24% or  
406 27% olivine ( $\pm 1\%$  ilmenite) are essentially identical due to low olivine-melt and ilmenite-melt  
407 partition coefficients. The resultant trace element compositions once again yield conflicting  
408 classifications (Figure 9). The La/Yb ratio is consistent with Type B1 basalts, while La/Sm is  
409 within the range of Type B2 basalts. The pre-cumulate abundances of La, Sm, and Cr are closest  
410 to Type B1 basalts. Modeled Yb and Eu abundances do not distinguish between Type B1 and B2

Revision 2

411 groups, and Co abundance is distinct only from Type B2 basalts. Therefore, either cumulate  
412 71597 resulted from accumulation in a new magma type, one or more of the INAA-determined  
413 REEs are not representative of the parent melt, or the simple model of olivine accumulation is  
414 insufficient. An argument for any of these three possibilities would remain equivocal if only bulk  
415 whole rock analyses were considered.

416       Equilibrium melt calculations theoretically yield compositions wherein mineral phases  
417 crystallized. Melt compositions (Figure 10) were calculated for each phase by dividing trace  
418 element abundances by mineral-specific partition coefficients for V, Cr, and the REEs (Table 5).  
419 Olivine partition coefficients were calculated using the relationship of D to bulk MgO of Bédard  
420 (2005). Other partition coefficients were determined at low  $fO_2$  (between IW-0 and IW-2) and  
421 with trace elements present at natural abundances (see references in Table 5). Equilibrium melts  
422 could be explained by a model in which fractional crystallization evolution is modified by  
423 olivine resorption (Figure 10b). Equilibrium liquid compositions calculated from the cores of  
424 augite are similar to light REEs (LREE) or elevated above the heavy REEs (HREE) compared to  
425 whole-rock values from Murali et al. (1977) (Figure 10c). The LREEs are more incompatible  
426 than HREEs in olivine, and so this discrepancy may result from an unaccounted for dilution of  
427 LREEs by olivine addition. Pigeonite equilibrium melts are similar to the compositional  
428 dispersion observed in plagioclase (Figure 10c), but the majority are depleted in Eu, as seen on  
429 Figure 10d. Pigeonite likely originated in olivine reaction rims after plagioclase crystallized,  
430 which limited available Eu. Plagioclase equilibrium compositions follow the expected positive  
431 correlation between La and Eu (Figure 10d).

432       Apollo 17 high-Ti basalts are classified primarily based on whole-rock trace element  
433 compositional variation. The trace elements obtained for olivine in 71597 are similar to olivines

Revision 2

434 found in other chemical groups. In addition, the paucity of olivine in Type B1 basalts is not  
435 conducive to such comparisons. Here, we utilize augite to trace source evolution, because augite  
436 crystallizes early in high-Ti basalts, and has sufficient incompatible trace element abundance for  
437 quantification by LA-ICP-MS analyses. On Figure 10d, the whole-rock fractionation trends of La  
438 and Eu in Apollo 17 high-Ti basalts are compared to the plagioclase and pyroxene equilibrium  
439 liquids. Pigeonite, as might be expected from a phase appearing late in the crystallization  
440 sequence after modification by partial resorption, does not appear to represent true liquid  
441 composition. Finally, the evolution from augite equilibrium melt to relatively late-stage  
442 plagioclase most closely follows a fractional crystallization trend from a Type B2 basalt source  
443 composition.

444

445

### **Implications**

446 Through careful characterization of sample petrography and mineral geochemistry, we  
447 are able to place constraints on the geochemical evolution of a unique Apollo sample and tie it to  
448 the Type B2 mare basalt suite. The Type B2 suite comprises nine fine-grained vitrophyric-  
449 olivine porphyritic basalts, and one plagioclase poikilitic basalt. Prior investigation suggesting a  
450 spread in Rb-Sr and Sm-Nd isotopes for whole-rock samples indicated the Type B2 basalts were  
451 affected by open system processes (Paces et al. 1991). We are not able to determine where  
452 olivine accumulation occurred, but it could have been in ponded melts at the base of or in the  
453 lunar crust, or within a thick high-Ti basalt flow. If it was the former, where multiple  
454 components were mixing while olivine was crystallizing, further study of olivine melt inclusions  
455 may be used to verify this process. If it was the latter case, then we would expect more coarse-

Revision 2

456 grained material represented in the Type B2 sample suite, which might be present but  
457 unrecognized in the Apollo sample collection.

458       Approximately one-third of high-Ti mare basalts returned by the Apollo 17 mission are  
459 designated as Type U or "unclassified" basalts. These have remained unclassified for 40+ years  
460 due to issues with obtaining representative bulk analyses, primarily due to small sample masses  
461 and coarse grain sizes. The approach used here has the potential to place petrogenetic constraints  
462 on these samples, and has demonstrated potential for classification and discrimination of Type U  
463 basalts within the current whole-rock classification scheme for Apollo 17 high-Ti basalts, and  
464 potentially identifying new basalt types. The Earth and the Moon share many similarities in  
465 eruption styles of basalts. The characterization of end-member samples like 71597 will be  
466 important for comparative analyses with the growing collection of mare basalt textures that have  
467 been defined through quantitative analysis. Finally, application of these microscale techniques  
468 will maximize the science potential of future robotic sample return missions to the Moon and  
469 other planetary bodies.

#### 470                           **Acknowledgments**

471       This research was funded by NASA Grant NNX09-AB92G to CRN. We thank lunar  
472 sample curators at the Johnson Space Center (NASA) for preparing the two new thin sections of  
473 71597 used in this study. Microprobe data collection was facilitated by Paul Carpenter at the  
474 University of Washington at St. Louis (St. Louis, MO) and Ian Steele at the University of  
475 Chicago (Chicago, IL). Tony Simonetti (University of Notre Dame, Notre Dame, IN) provided  
476 LA-ICP-MS training, support, and advice at MITERAC. We thank James D Day and Bruce  
477 Marsh for critical comments on an earlier version of this manuscript. Additional reviews by Arya  
478 Udry and Tabb Prissel, and associate editor Steve Simon further improved the paper.

## References

- 479
- 480 van Achterbergh, E., Ryan, C.G., Jackson, S.E., and Griffin, W.L. (2001) Data reduction  
481 software for LA-ICP-MS: Appendix. In P.J. Sylvester, Ed., Laser ablation-ICP-mass  
482 spectrometry in the Earth Sciences: Principles and applications, Vol. 29, pp. 239–243.  
483 Mineralogical Association of Canada, Short Course Series.
- 484 Alexander, L., Snape, J.F., Crawford, I.A., Joy, K.H., and Downes, H. (2014) Searching for  
485 nonlocal lithologies in the Apollo 12 regolith: A geochemical and petrological study of  
486 basaltic coarse fines from the Apollo lunarsoil sample 12023,155. *Meteoritics & Planetary  
487 Science*, 49, 1288–1304.
- 488 Bédard, J.H. (2005) Partitioning coefficients between olivine and silicate melts. *Lithos*, 83, 394–  
489 419.
- 490 Bindeman, I.N., Davis, A.M., and Drake, M.J. (1998) Ion microprobe study of plagioclase-basalt  
491 partition experiments at natural concentration levels of trace elements. *Geochimica et  
492 Cosmochimica Acta*, 62, 1175–1193.
- 493 Burkhard, D.J.M. (2005) Nucleation and growth rates of pyroxene, plagioclase, and Fe-Ti oxides  
494 in basalt under atmospheric conditions. *European Journal of Mineralogy*, 17, 675–686.
- 495 Cabane, H., Laporte, D., and Provost, A. (2005) An experimental study of Ostwald ripening of  
496 olivine and plagioclase in silicate melts: Implications for the growth and size of crystals in  
497 magmas. *Contributions to Mineralogy and Petrology*, 150, 37-53.
- 498 Cashman, K.V., and Marsh, B.D. (1988) Crystal size distribution (CSD) in rocks and the kinetics  
499 and dynamics of crystallization II: Makaopuhi lava lake. *Contributions to Mineralogy and  
500 Petrology*, 99, 292–305.
- 501 Cushing, J.A., Taylor, G.J., Norman, M.D., and Keil, K. (1999) The granulitic impactite suite:

Revision 2

- 502 Impact melts and metamorphic breccias of the early lunar crust. *Meteoritics & Planetary*  
503 *Science*, 34, 185–195.
- 504 Day, J.M.D., and Taylor, L.A. (2007) On the structure of mare basalt lava flows from textural  
505 analysis of the LaPaz Icefield and Northwest Africa 032 lunar meteorites. *Meteoritics &*  
506 *Planetary Science*, 42, 3–17.
- 507 Delano, J.W. (1980) Chemistry and liquidus phase relations of Apollo 15 red glass: Implications  
508 for the deep lunar interior. *Proceedings of the 11<sup>th</sup> Lunar and Planetary Science Conference*,  
509 251-288.
- 510 Donohue, P.H., and Neal, C.R. (2015) Quantitative textural analysis of ilmenite in Apollo 17  
511 high-titanium mare basalts. *Geochimica et Cosmochimica Acta*, 149, 115–130.
- 512 Dungan, M.A., and Brown, R.W. (1977) The petrology of the Apollo 12 ilmenite basalt suite.  
513 *Proceedings of the 8<sup>th</sup> Lunar Science Conference*, 1339–1381.
- 514 Dygert, N., Liang, Y., and Hess, P.C. (2013) The importance of melt TiO<sub>2</sub> in affecting major and  
515 trace element partitioning between Fe-Ti oxides and lunar picritic glass melts. *Geochimica et*  
516 *Cosmochimica Acta*, 106, 134–151.
- 517 Dymek, R.F., Albee, A.L., and Chodos, A.A. (1975) Comparative mineralogy and petrology of  
518 Apollo 17 mare basalts: Samples 70215, 71055, 74255, and 75055. *Proceedings of the 6<sup>th</sup>*  
519 *Lunar Science Conference*, 49–77.
- 520 El Goresy, A., and Ramdohr, P. (1975) Subsolidus reduction of lunar opaque oxides: Textures,  
521 assemblages, geochemistry, and evidence for a late-stage endogenic gaseous mixture.  
522 *Proceedings of the 6<sup>th</sup> Lunar Science Conference*, 729–745.
- 523 Fagan, A.L., Neal, C.R., Simonetti, A., Donohue, P.H., and O'Sullivan, K.M. (2013)  
524 Distinguishing between Apollo 14 impact melt and pristine mare basalt samples by

Revision 2

- 525 geochemical and textural analyses of olivine. *Geochimica et Cosmochimica Acta*, 106, 429–  
526 445.
- 527 Hallis, L.J., Anand, M., and Strekopytov, S. (2014) Trace-element modelling of mare basalt  
528 parental melts: Implications for a heterogeneous lunar mantle. *Geochimica et Cosmochimica*  
529 *Acta*, 134, 289–316.
- 530 Haskin, L.A., and Korotev, R.L. (1977) Test of a model for trace element partition during closed-  
531 system solidification of a silicate liquid. *Geochimica et Cosmochimica Acta*, 41, 921–939.
- 532 Haskin, L.A., Jacobs, J.W., Brannon, J.C., and Haskin, M.A. (1977) Compositional dispersions  
533 in lunar and terrestrial basalts. *Proceedings of the 8<sup>th</sup> Lunar and Planetary Science*  
534 *Conference*, 1731-1750.
- 535 Higgins, M.D. (2000) Measurement of crystal size distributions. *American Mineralogist*, 85,  
536 1105–1116.
- 537 Higgins, M.D. (2002) Closure in crystal size distributions (CSD), verification of CSD  
538 calculations, and the significance of CSD fans. *American Mineralogist*, 87, 171–175.
- 539 Higgins, M.D. (2006) Verification of ideal semi-logarithmic, lognormal or fractal crystal size  
540 distributions from 2D datasets. *Journal of Volcanology and Geothermal Research*, 154, 8–16.
- 541 Higgins, M.D., and Roberge, J. (2003) Crystal size distribution of plagioclase and amphibole  
542 from Soufrière Hills Volcano, Montserrat: Evidence for dynamic crystallization–textural  
543 coarsening cycles. *Journal of Petrology*, 44, 1401–1411.
- 544 Hodges, F.N., and Kushiro, I. (1974) Apollo 17 petrology and experimental determination of  
545 differentiation sequences in model moon compositions. *Proceedings of the 5<sup>th</sup> Lunar*  
546 *Conference*, 505–520.
- 547 Hui, H., Oshrin, J.G., and Neal, C.R. (2011) Investigation into the petrogenesis of Apollo 14



- 548 high-Al basaltic melts through crystal stratigraphy of plagioclase. *Geochimica et*  
549 *Cosmochimica Acta*, 75, 6439–6460.
- 550 Irving A. J., Merrill R. B. and Singleton D. E. (1978) Experimental partitioning of rare earth  
551 elements and scandium among armalcolite, ilmenite, olivine and mare basalt liquid.  
552 *Proceedings of the 9<sup>th</sup> Lunar and Planetary Science Conference*, 601–612.
- 553 Jerram, D.A., Cheadle, M.J., Hunter, R.H., and Elliott, M.T. (1996) The spatial distribution of  
554 grains and crystals in rocks. *Contributions to Mineralogy and Petrology*, 125, 60–74.
- 555 Jerram, D.A., Cheadle, M.J., and Philpotts, A.R. (2003) Quantifying the building blocks of  
556 igneous rocks: Are clustered crystal frameworks the foundation? *Journal of Petrology*, 44,  
557 2033–2051.
- 558 Jerram, D.A., Davis, G.R., Mock, A., Charrier, A., and Marsh, B.D. (2010) Quantifying 3D  
559 crystal populations, packing and layering in shallow intrusions: A case study from the  
560 Basement Sill, Dry Valleys, Antarctica. *Geosphere*, 6, 537–548.
- 561 Jolliff, B.L., Korotev, R.L., Zeigler, R.A., and Floss, C. (2003) Northwest Africa 773: Lunar  
562 mare breccia with a shallow-formed olivine-cumulate component, inferred very-low-Ti  
563 (VLT) heritage, and a KREEP connection. *Geochimica et Cosmochimica Acta*, 67, 4857–  
564 4879.
- 565 Klemme, S., Günther, D., Hametner, K., Prowatke, S. and Zack, T. (2006) The partitioning of  
566 trace elements between ilmenite, ulvospinel, armalcolite and silicate melts with implications  
567 for the early differentiation of the moon. *Chemical Geology*, 234, 251–263.
- 568 Laul, J.C., Schmitt, R.A., Robyn, M., and Goles, G.G. (1975) Chemical Composition of 18  
569 Apollo 17 Rake Basalts and One Basalt Breccia. *Proceedings of the 6<sup>th</sup> Lunar and Planetary*  
570 *Science Conference*, 492–493.

Revision 2

- 571 Longhi, J., Walker, D., and Hays, J.F. (1978) The distribution of Fe and Mg between olivine and  
572 lunar basaltic liquids. *Geochimica et Cosmochimica Acta*, 42, 1545-1558.
- 573 Mallmann, G., and O'Neill, H.S.C. (2009) The crystal/melt partitioning of V during mantle  
574 melting as a function of oxygen fugacity compared with some other elements (Al, P, Ca, Sc,  
575 Ti, Cr, Fe, Ga, Y, Zr and Nb). *Journal of Petrology*, 50, 1765–1794.
- 576 Marsh, B.D. (1988) Crystal size distribution (CSD) in rocks and the kinetics and dynamics of  
577 crystallization I. Theory. *Contributions to Mineralogy and Petrology*, 99, 277–291.
- 578 Marsh, B.D. (1998) On the interpretation of crystal size distributions in magmatic systems.  
579 *Journal of Petrology*, 39, 553–599.
- 580 Martin, V.M., Pyle, D.M., and Holness, M.B. (2006) The role of crystal frameworks in the  
581 preservation of enclaves during magma mixing. *Earth and Planetary Science Letters*, 248,  
582 787–799.
- 583 Masuda, A., Tanaka, T., Nakamura, N., and Kurasawa, H. (1974) Possible REE anomalies of  
584 Apollo 17 REE patterns. *Proceedings of the 5<sup>th</sup> Lunar Conference*, 2, 1247–1253.
- 585 McCallum, I.S., and Charette, M.P. (1978) Zr and Nb partition coefficients: Implications for the  
586 genesis of mare basalts, KREEP, and sea floor basalts. *Geochimica et Cosmochimica Acta*,  
587 42, 859–869.
- 588 McDonough, W.F. and Sun, S.-S. (1995) The composition of the Earth. *Chemical Geology*, 120,  
589 223–253.
- 590 Morgan, D.J., and Jerram, D.A. (2006) On estimating crystal shape for crystal size distribution  
591 analysis. *Journal of Volcanology and Geothermal Research*, 154, 1–7.
- 592 Murali, A.V., Ma, M.-S., and Schmitt, R.A. (1977) Chemistry of 30 Apollo 17 rake basalts;  
593 71597 a product of partial olivine accumulation. *Abstracts of the 8<sup>th</sup> Lunar and Planetary*

Revision 2

- 594 Science Conference, 703–704.
- 595 Neal, C.R. (2001) Interior of the Moon: The presence of garnet in the primitive deep lunar  
596 mantle. *Journal of Geophysical Research*, 106, 27865–27886.
- 597 Neal, C.R., and Taylor, L.A. (1990) Modeling of lunar basalt petrogenesis: Sr isotope evidence  
598 from Apollo 14 high-alumina basalts. *Proceedings of the 20<sup>th</sup> Lunar and Planetary Science*  
599 *Conference*, 101–108.
- 600 Neal, C.R., and Taylor, L.A. (1993) *Catalog of Apollo 17 Rocks Volume 2 - Central Valley, Part*  
601 *1*, 472 pp. NASA.
- 602 Neal, C.R., Taylor, L.A., Hughes, S.S., and Schmitt, R.A. (1990) The significance of fractional  
603 crystallization in the petrogenesis of Apollo 17 Type A and B high-Ti basalts. *Geochimica et*  
604 *Cosmochimica Acta*, 54, 1817–1833.
- 605 Neal, C.R., Hacker, M.D., Snyder, G.A., Taylor, L.A., Liu, Y.-G., and Schmitt, R.A. (1994)  
606 Basalt generation at the Apollo 12 site, Part 2: Source heterogeneity, multiple melts, and  
607 crustal contamination. *Meteoritics*, 29, 349–361.
- 608 Neal, C.R., Donohue, P.H., Fagan, A.L., O'Sullivan, K.M., Oshrin, J., and Roberts, S. (2015)  
609 Distinguishing between basalts produced by endogenic volcanism and impact processes: A  
610 non-destructive method using quantitative petrography of lunar basaltic samples. *Geochimica*  
611 *et Cosmochimica Acta*, 148, 62–80.
- 612 Paces J.B., Nakai S., Neal C.R., Taylor L.A., Halliday A.N. and Lee D.-C. (1991) A strontium  
613 and neodymium isotopic study of Apollo 17 high-Ti mare basalts: Resolution of ages,  
614 evolution of magmas, and origins of source heterogeneities. *Geochimica et Cosmochimica*  
615 *Acta*, 55, 2025–2043.
- 616 Papike, J.J., Bence, A.E., and Lindsley, D.H. (1974) Mare basalts from the Taurus-Littrow

Revision 2

- 617 region of the moon. Proceedings of the 5<sup>th</sup> Lunar Conference, 471–504.
- 618 Papike, J.J., Hodges, F.N., Bence, A.E., Cameron, M., and Rhodes, J.M. (1976) Mare basalts:  
619 Crystal chemistry, mineralogy, and petrology. Reviews of Geophysics and Space Physics, 14,  
620 475–540.
- 621 Pearce, N.J., Perkins, W.T., Westgate, J.A., Gorton, M.P., Jackson, S.E., Neal, C.R., and  
622 Chenery, S.P. (1997) A compilation of new and published major and trace element data for  
623 NIST SRM 610 and NIST SRM 612 glass reference materials. Geostandards Newsletter, 21,  
624 115–144.
- 625 Rhodes, J.M., Hubbard, N.J., Wiesmann, H., Rodgers, K.V., Brannon, J.C., and Bansal, B.M.  
626 (1976) Chemistry, classification, and petrogenesis of Apollo 17 mare basalts. Proceedings of  
627 the 7<sup>th</sup> Lunar Science Conference, 1467–1489.
- 628 Rhodes, J.M., Brannon, J.C., Rodgers, K.V., Blanchard, D.P., and Dungan, M.A. (1977)  
629 Chemistry of Apollo 12 mare basalts: Magma types and fractionation processes. Proceedings  
630 of the 8<sup>th</sup> Lunar Science Conference, 1305–1338.
- 631 Ryder, G. (1985) Catalog of Apollo 15 Rocks Part 2. 15306-15468. Curatorial Branch  
632 Publication, 72, 443 pp. NASA.
- 633 Ryder, G. (1990) A distinct variant of high-titanium mare basalt from the Van Serg core, Apollo  
634 17 landing site. Meteoritics, 25, 249–258.
- 635 Ryder, G., and Schuraytz, B.C. (2001) Chemical variation of the large Apollo 15 olivine-  
636 normative mare basalt rock samples. Journal of Geophysical Research, 106, 1435-1451.
- 637 Schnare, D.W., Day, J.M.D., Norman, M.D., Liu, Y., and Taylor, L.A. (2008) A laser-ablation  
638 ICP-MS study of Apollo 15 low-titanium olivine-normative and quartz-normative mare  
639 basalts. Geochimica et Cosmochimica Acta, 72, 2556–2572.

Revision 2

- 640 Schneider, C.A., Rasband, W.S., and Eliceiri, K.W. (2012) NIH Image to ImageJ: 25 years of  
641 image analysis. *Nature Methods*, 9, 671–675.
- 642 Shih, C.-Y., Wiesmann, H., Bansal, B.M., Brannon, J.C., and Haskin, L.A. (1975) On the origin  
643 of high-Ti mare basalts. *Proceedings of the 6<sup>th</sup> Lunar Science Conference*, 1255–1285.
- 644 Stanin, F.T., and Taylor, L.A. (1980) Armalcolite: An oxygen fugacity indicator. *Proceedings of*  
645 *the 11<sup>th</sup> Lunar and Planetary Science Conference*, 117–124.
- 646 Sun, C., and Liang, Y. (2012) Distribution of REE between clinopyroxene and basaltic melt  
647 along a mantle adiabat: effects of major element composition, water, and temperature.  
648 *Contributions to Mineralogy and Petrology*, 163, 807–823.
- 649 Taylor, L.A., Shervais, J.W., Hunter, R.H., Shih, C.-Y., Bansal, B.M., Wooden, J.L., Nyquist,  
650 L.E., and Laul, L.C. (1983) Pre-4.2 AE mare-basalt volcanism in the lunar highlands. *Earth*  
651 *and Planetary Science Letters*, 66, 33–47.
- 652 Usselman, T.M., Lofgren, G.E., Donaldson, C.H., and Williams, R.J. (1975) Experimentally  
653 reproduced textures and mineral chemistries of high-titanium mare basalts. *Proceedings of*  
654 *the 6<sup>th</sup> Lunar Science Conference*, 997–1020.
- 655 Usselman, T.M., and Lofgren, G.E. (1976) The phase relations, textures, and mineral chemistries  
656 of high-titanium mare basalts as a function of oxygen fugacity and cooling rate. *Proceedings*  
657 *of the 7<sup>th</sup> Lunar Science Conference*, 1345–1363.
- 658 Vinet, N., and Higgins, M.D. (2010) Magma solidification processes beneath Kilauea Volcano,  
659 Hawaii: A quantitative textural and geochemical study of the 1969-1974 Mauna Ulu lavas.  
660 *Journal of Petrology*, 51, 1297–1332.
- 661 Vobecký, M., Frána, J., Bauer, J., Řanda, Z., Benada, J., and Kuncíř, J. (1971) Radioanalytical  
662 determination of elemental compositions of lunar samples. *Proceedings of the 2<sup>nd</sup> Lunar*

Revision 2

- 663 Science Conference, 2, 1291–1300.
- 664 Walker, D., Longhi, J., and Hays, J.F. (1976) Heterogeneity in titaniferous lunar basalts. Earth  
665 and Planetary Science Letters, 30, 27–36.
- 666 Warner, R.D., Keil, K., Prinz, M., Laul, J.C., Murali, A.V., and Schmitt, R.A. (1975)  
667 Mineralogy, petrology, and chemistry of mare basalts from Apollo 17 rake samples.  
668 Proceedings of the 6<sup>th</sup> Lunar Science Conference, 193–220.
- 669 Warner, R.D., Berkley, J.L., Mansker, W.L., Warren, R.G., and Keil, K. (1976a) Electron  
670 microprobe analyses of spinel, Fe-Ti oxides and metal from Apollo 17 rake sample mare  
671 basalts. Spec. Pub. #16, UNM Institute of Meteoritics, Albuquerque, 114 pp.
- 672 Warner, R.D., Warren, R.G., Mansker, W.L., Berkley, J.L., and Keil, K. (1976b) Electron  
673 microprobe analyses of olivine, pyroxene and plagioclase from Apollo 17 rake sample mare  
674 basalts, Spec. Pub. #15, UNM Institute of Meteoritics, Albuquerque, 121 pp.
- 675 Warner, R.D., Keil, K., and Taylor, G.J. (1977) Coarse-grained basalt 71597: A product of  
676 partial olivine accumulation. Proceedings of the 8<sup>th</sup> Lunar Science Conference, 1429–1442.
- 677 Warner, R.D., Taylor, G.J., Conrad, G.H., Northrop, H.R., Barker, S., Keil, K., Ma, M.-S., and  
678 Schmitt, R.A. (1979) Apollo 17 high-Ti mare basalts: New bulk compositional data, magma  
679 types, and petrogenesis. Proceedings of the 10<sup>th</sup> Lunar and Planetary Science Conference,  
680 225–247.
- 681

682 **Figure Captions**

683 Figure 1. Plane-polarized light views and composites of traced phases of the two new thin  
684 sections of 71597. (a) 71597,12 and (b) composite of traced ilmenite, olivine, plagioclase, and  
685 pyroxene. Note pyroxene was only traced for half of the section. For (c) section 71597,13, only  
686 (d) ilmenite and olivine were traced. The more subdued color of olivine and pyroxene on the  
687 bottom half of 71597,13 is due to the lower thickness of the thin section. Crystals intersecting the  
688 edge of the sections were not traced. Gray areas in (b) and (d) represent the sample area.

689 Figure 2. Crystal size distribution profiles for 71597,12 and ,13. (a) Olivine CSD profiles appear  
690 to be multiply kinked, and (b) ilmenite CSDs are concave upward. The CSD profiles are sub-  
691 linear for (c) pyroxene and (d) plagioclase.

692 Figure 3. R-value (relative ordering) versus Porosity (% matrix) for phases in Apollo 17 high-Ti  
693 basalts (open symbols; Donohue and Neal 2015) and basalt 71597,12 (filled symbols). RSDL =  
694 Random Sphere Distribution Line for modeled population of uniform spheres; points to the left  
695 of the Touching Framework line (TF) form a touching framework of crystals. Besides olivine in  
696 71597, plagioclase in coarse-grained Type A basalt 75015 is the only other non-pyroxene phase  
697 to approach a clustered crystal distribution. The processes resulting in trends for related samples  
698 are included schematically. Figure after Jerram et al. 2003.

699 Figure 4. Ranges of (a) olivine Fo and (b) plagioclase An compositions observed in 71597  
700 compared to literature values for individual samples of other lunar basalt types. Data from Fagan  
701 et al. (2013), Hallis et al. (2014), Schnare et al. (2008), and Neal and Taylor (1990).

702 Figure 5. Element variation diagrams for large olivine interiors (filled) and rims (open symbols)  
703 as well as matrix olivine depicting (a) decreasing V (ppm) with melt evolution, and (b)

Revision 2

704 corresponding increase in Y (ppm) abundance. Vertical lines indicate  $1\sigma$  errors. Multiple  
705 analyses of individual crystals are connected with a gray line.

706 Figure 6. Olivine forsterite variability versus (a) Ti/V and (b) Cr/Y versus olivine forsterite  
707 contents. Fields drawn from literature: Apollo 12 (A12) ilmenite basalts, pigeonite basalts,  
708 olivine basalts, Apollo 14 (A14) Groups A, B, and C basalts, Apollo 14 olivine vitrophyres  
709 (OV), and Apollo 17 sample 74275 from Fagan et al. (2013); Apollo 15 (A15) olivine normative  
710 and quartz normative basalts from Schnare et al. (2008).

711 Figure 7. Ilmenite major and trace element variation diagrams.  $1\sigma$  errors for trace elements  
712 indicated for each point where larger than the symbol.

713 Figure 8. (a) Composition of pyroxene projected onto pyroxene quadrilateral with data from  
714 Warner et al. (1977) for comparison. (b) REE profiles of augite, pigeonite, and plagioclase of  
715 71597 are typical of Apollo 17 basalts. Whole-rock values from 71597,1 (Murali et al. 1977).  
716 Values for CI chondrite from McDonough and Sun (1995).

717 Figure 9. Compositional fields drawn from bulk rock analyses of Apollo 17 high-Ti basalts of (a)  
718 TiO<sub>2</sub> (wt.%) versus MgO (wt.%), (b) Sm (ppm) versus Cr/La, (c) La/Sm versus La (ppm), and  
719 (d) Hf (ppm) versus La/Yb. Gray shaded circles are compositions resulting from 24% (dark gray)  
720 and 27% (light gray) olivine subtraction from analysis of 71597,1 (black circle, Murali et al.  
721 1977). Gray triangle represents subtraction of 27% olivine and 1% ilmenite.

722 Figure 10. Element variation diagrams for calculated equilibrium melts from crystal interiors  
723 (filled symbols) and rims (open symbols). (a) Mg# versus V (ppm). (b) Cr/Y versus Cr (ppm)  
724 with inferred magma compositional path shown (dashed line). (c) Chondrite-normalized  
725 pyroxene and plagioclase equilibrium melt REE profiles compared to reported whole-rock and



Revision 2

726 olivine subtracted compositions. (d) La versus Eu correlation of whole-rock compositions from  
727 each group, and equilibrium liquid compositions of augite, pigeonite, and plagioclase. Fractional  
728 crystallization (FC) paths for Types B1 and B2 basalts are from Neal et al. (1990) to 70%  
729 crystallization. Two analyses of high-REE plagioclase are not shown, as they represent extreme  
730 fractionation during late stage cooling. Calculations for removal of 24% olivine and 27% olivine  
731 + 1% ilmenite (not shown) are within uncertainty of the -27% olivine on (c) and (d). Open  
732 symbols in (a), (b), and (d) represent rim analyses. Literature bulk La and Eu values from  
733 (Masuda et al. 1974; Laul et al. 1975; Shih et al. 1975; Warner et al. 1975; Rhodes et al. 1976;  
734 Murali et al. 1977; Warner et al. 1979; Neal et al. 1990; Neal 2001).

735

736

### **Supplementary Material**

737

738 Supplementary Table S1 (Deposit item)

739

740

741

**Tables**

742 Table 1. Crystal size distribution data for major phases.

Phase split(s)	Area (mm <sup>2</sup> )	Crystals	vol %	Slope1	y-int1	Slope2	y-int2	shape parameters	R2	NND average	SDP R value
<b>Olivine</b>											
,12	102.2	118	16.4%	-9.04 ± 1.70	4.55 ± 0.49	-2.48 ± 0.10	1.27 ± 0.12	1:1.4:2	0.80	0.345	0.59
,13	61.7	43	19.2%	-8.47 ± 1.15	4.15 ± 0.35	-2.07 ± 0.13	0.81 ± 0.25	1:1.5:2.3	0.81	<i>n.a.</i>	<i>n.a.</i>
,12 + ,13	163.9	161	17.5%	-13.41 ± 0.45	5.12 ± 0.12	-1.76 ± 0.39	0.09 ± 0.79	1:1.4:1.9	0.84	<i>n.a.</i>	<i>n.a.</i>
<b>Ilmenite</b>											
,12	102.2	482	5.7%	-2.60 ± 0.58	3.86 ± 0.30	-1.53 ± 0.17	2.29 ± 0.49	1:1.25:7	0.78	0.116	0.76
,13	95.7	393	6.9%	-3.06 ± 0.10	4.08 ± 0.04	-1.63 ± 0.21	1.73 ± 0.59	1:1.7:6	0.73	0.113	0.65
,12 + ,13	197.9	875	6.3%	-2.28 ± 0.30	3.57 ± 0.15	-1.22 ± 0.13	1.67 ± 0.53	1:1.25:7	0.77	<i>n.a.</i>	<i>n.a.</i>
<b>Plagioclase</b>											
,12	102.2	286	10.9%	-2.25 ± 0.13	2.93 ± 0.20	-	-	1:1.7:4.5	0.79	0.260	0.91
<b>Pyroxene</b>											
,12	102.2	362	35.5%	-3.51 ± 0.29	4.77 ± 0.35	-	-	1:1.6:2.9	0.81	0.181	1.03

743 n.a.: not applicable. Vol % = volume percent.

744 Slope# and y-int# = slope and intercept of portions of CSD profiles representing different size populations.

745 NND: nearest neighbor distance (mm) to crystal of same phase.

746

747

748 Table 2. Average olivine and Fe-Ti oxide mineral chemistry for 71597 and for mare basalt groups.

Phase	Large olivine		Matrix olivine		Ilmenite	Armalcolite	A17 Type A, B1, B2, C, U		A11 low-K, high-K		A12 Ilm, Ol, and Pigeonite suites		A14 high-Al and Ol. Vitrophyre		A15 KREEP & Ol normative					
	core	2 $\sigma$	rim	2 $\sigma$	core	2 $\sigma$	average	2 $\sigma$	average	2 $\sigma$	Olivine	Ilmenite	Olivine	Ilmenite	Olivine	Ilmenite	Olivine	Ilmenite		
<i>n</i> =	8		8		4		14		2											
<i>wt. %</i>																				
SiO <sub>2</sub>	37.7	0.7	37.3	0.8	36.9	1.6					24.7 - 41.0	0.01 - 0.38	29.2 - 38.6	0.12 - 0.23	33.4 - 39.9	0.03 - 8.90	35.7 - 42.3	0.16	27.2 - 48.2	b.d. - 3.42
TiO <sub>2</sub>							54.4	2.0	73.2	1.4	0.03 - 0.48	50.6 - 56.1		52.1 - 53.0	b.d. - 0.20	43.7 - 54.3	0.01 - 0.15	53.24	0.01 - 1.03	39.7 - 52.9
Al <sub>2</sub> O <sub>3</sub>							0.04	0.02	2.03	0.04	b.d. - 0.47	b.d. - 0.62	b.d. - 0.3		b.d. - 0.74	b.d. - 1.13	b.d. - 0.21	0.09		0.03 - 1.28
Cr <sub>2</sub> O <sub>3</sub>	0.21	0.06	0.18	0.08	0.15	0.02	0.73	0.26	1.39	0.15	0.04 - 0.37	0.15 - 1.11	0.02 - 0.28	0.52 - 2.12	0.05 - 0.74	b.d. - 0.75	b.d. - 1.39	0.35	b.d. - 0.51	b.d. - 1.08
FeO	25.4	2.9	27.8	2.6	30.7	2.40	39.9	2.5	17.6	1.1	15.6 - 46	34.8 - 46.4	25.4 - 68.7	44.4 - 45.1	20.7 - 65.3	41.7 - 47.3	11.6 - 41.8	45.3	22.6 - 67.8	42.5 - 56.7
MnO	0.28	0.05	0.29	0.05	0.33	0.12	0.37	0.07	0.07	0.04	0.18 - 0.48	0.3 - 0.59	0.22 - 1.10	0.45	b.d. - 0.52	0.27 - 0.43	0.10 - 0.42	0.47	0.26 - 0.75	0.19 - 0.39
MgO	36.1	3.0	34.1	2.4	31.9	2.37	4.47	0.95	5.54	0.13	19.5 - 44	0.1 - 8.7	0.5 - 36.5	0.75 - 1.35	3.54 - 40.1	b.d. - 3.17	23.6 - 48.7	0.72	0.45 - 34.4	0.04 - 2.12
CaO	0.26	0.02	0.26	0.03	0.26	0.03					0.2 - 0.78	0.06 - 0.44	0.26 - 0.33	0.01 - 0.10	0 - 0.34	b.d. - 2.51	0.03 - 0.85	0.05	0.24 - 11.7	0.004 - 0.36
TOTAL	100.05	0.73	100.07	0.94	100.26	1.14	99.91	0.96	99.85	2.22										
Ol. Fo%	72	4	69	3	65	3					37 - 82		1 - 73.3		9 - 78		50 - 88		1.22 - 70.5	
Ilm Mg#							17	3	36	2		0.22 - 29		2.9 - 5.1		0 - 11.9		2.8		0.10 - 8.12
<i>ppm</i>																				
Sc	15	8	14	9	18	7	101	20	233	24	7.73 - 15.0	83 - 104		123	4.42 - 85.6		1.31 - 37.18		7.9 - 44.5	17.2 - 32.9
Ti	462	142	417	112	584	357					219 - 962				102 - 865		30.7 - 3028		122 - 2930	
V	43	21	33	23	24	13	412	254	1399	118	26.4 - 51.5			107	20.5 - 157		9.95 - 121		27.1 - 316	47.5 - 153
Cr	1299	642	1061	514	946	489	3741	2349	7655	1074	991 - 1991	132 - 163			530 - 4840		140 - 3698		675 - 6047	532 - 1601
Mn	2129	441	2196	436	2581	912	2391	725	753	90	1358 - 2202				1626 - 5208		589 - 3245		1970 - 4028	1841 - 3309
Co	65	16	63	28	71	26	8	9	20	2	39.5 - 56.8	20.9		24	80.6 - 238		14.7 - 85.6		86.2 - 148	22.7 - 29.2
Ni	35	20	23	6							21.7 - 68.8				6.55 - 500		4.17 - 362		38.8 - 203	4.4 - 6.3
Zn							3	1							1.58 - 6.94					
Y	3	3	4	3	5	3					0.18 - 2.14				0.14 - 3.66		0.03 - 72.1		0.2 - 4.7	1.7 - 8.2
Zr			2		2		426	843	233	4					b.d. - 0.65				0.1 - 3.7	289 - 1127
Nb							51	178	32	1					b.d. - 0.37				0 - 0.1	43.2 - 75.8
Hf							19	50	12	2		17.4		11	b.d. - 0.02				0 - 0.2	6.9 - 18.1
Ta							3	7	3	4		4.9			b.d.				0	4.0 - 5.9
Sr							2	3	b.d.						b.d. - 0.43				0 - 3.0	2.1 - 2.3

749 b.d.: below detection limit; 2 $\sigma$  = two standard deviation of average value listed.

750 Literature data from Vobecký et al. (1971); Papike et al. (1974, 1976); Dymek et al. (1975); Warner et al. (1975, 1976a, 1976b, 1977);

751 Walker et al. (1976); Haskin and Korotev (1977); McCallum and Charette (1978); Neal et al. (1990); Schnare et al. (2008); Fagan et

752 al. (2013); Alexander et al. (2014); and Hallis et al. (2014).

753

754

755

756 Table 3. Average compositions of pyroxene and plagioclase compared to major mare basalt groups.

Phase Analysis	Augite		Pigeonite		Plagioclase		A11 low-K and high-K		A12 Ilm, Ol, Plag basalts		A14 KREEP and high-AI		A15 KREEP and ONB		A17 Type A, B1, B2, C, U	
	average	2σ	average	2σ	average	2σ	Pyroxene	Plagioclase	Pyroxene	Plagioclase	Pyroxene	Feldspar	Pyroxene	Feldspar	Pyroxene	Feldspar
n =	13		5		19											
wt. %																
SiO <sub>2</sub>	48.7	3.6	51.6	3.6	47.3	1.5	44.1 - 52.5	45.7 - 53.3	45.0 - 53.5	44.3 - 48.2	45.3 - 51.3	42.8 - 49.5	41.2 - 54.0	43.1 - 48.5	38.1 - 78.5	45.5 - 52.4
TiO <sub>2</sub>	3.52	1.79	1.33	1.79	0.13	0.07	0.72 - 3.74	0.5	0.35 - 2.64	0.03 - 0.16	0.84 - 1.62	0.02 - 0.11	0.19 - 3.99		0.26 - 14.1	0.03 - 0.32
Al <sub>2</sub> O <sub>3</sub>	4.78	2.75	1.67	2.75	32.7	1.4	0.57 - 5.25	17.2 - 34.5	0.66 - 7.90	30.9 - 35.7	1.20 - 3.01	31.3 - 36.0	0.26 - 11.9	30.1 - 34.6	0.42 - 23.4	0.11 - 34.5
Cr <sub>2</sub> O <sub>3</sub>	0.91	0.40	0.39	0.40	-		0 - 0.61	0.04	0 - 1.54		0 - 0.73		0 - 1.44		0.04 - 1.12	
FeO	9.39	3.77	18.9	3.8	0.45	0.18	9.6 - 45.8	0.30 - 2.8	12.9 - 46.5	0.49 - 1.85	15.4 - 34.7	0.07 - 0.99	12.9 - 45.9	0.37 - 1.06	2.31 - 48	0.28 - 32.9
MnO	0.22	0.10	0.36	0.10	-		0 - 0.67	0.05	0 - 0.56	<0.05	0 - 0.53		0.18 - 0.80		0 - 0.62	
MgO	14.4	2.7	18.8	2.7	0.30	0.10	1.40 - 22.0	0.07 - 2.5	0.29 - 24.3	0.01 - 0.51	0.57 - 21.2	0.03 - 0.38	0.15 - 26.3	0.15 - 1.16	0.27 - 24.4	0.01 - 0.31
CaO	17.8	5.0	6.61	5.02	17.2	1.0	3.52 - 18.8	11.7 - 18.6	2.61 - 16.9	16.3 - 19.2	4.37 - 18.2	15.6 - 19.4	2.02 - 18.2	16.3 - 19.0	0.75 - 20.7	0.11 - 17.4
Na <sub>2</sub> O	0.07	0.04	0.02	0.04	1.35	0.32	0 - 0.12	0.55 - 2.70	0 - 0.05	0.40 - 1.72	0 - 0.09	0.41 - 2.21	0 - 0.12	0.70 - 1.67	0 - 0.55	0.78 - 2.45
TOTAL	99.86	1.17	99.78	1.17	99.41	1.51										
Mg#	73	4	64	4	55	13	5 - 73	18 - 54	1 - 72	1 - 54			18 - 75			
En	44	6	55	6	-		0.6 - 63.4		0.41 - 67.0		5.8 - 63.7		1.9 - 80.1		0.9 - 67.1	
Fs	16	6	31	6	-				22.1 - 80.5						13.3 - 91.1	
Wo	40	12	14	12	-		0.55 - 43.5		6.55 - 42.2		7.5 - 33.7		2.6 - 36.2		5 - 49.3	
An	-	-	-	-	88	3		72.2 - 94.0		82.3 - 95.6		65.1 - 96.2		81.4 - 93.4		35.6 - 93.4
ppm																
Sc	196	270	220	270	b.d.		133	10.1	32 - 207	2.8 - 7.1			21.6 - 168	1.7 - 3.5	54 - 129	1
Ti	22566	10445	8432	10445	857	290			2840 - 16400	266 - 825			1409 - 12596	166 - 418		
Cr	4521	1617	1945	1617	6	3			132 - 22000	1.5 - 26.7			20.2 - 18636	2.4 - 13.9		
Mn	1437	483	591	483	57	7			760 - 8480	50.5 - 107			416 - 8191	42.7 - 83.2		
Co	10	5	12	5	0.4	0.3	22	8.5	10 - 159	b.d. - 1.7			7.7 - 140	0.3 - 1.6	14 - 24	0.84
Ga	1.2	0.4	0.7	0.4	11	26						2.3 - 85	0.3 - 2.3	4.2 - 13.3		
Sr	9.7	3.5	4.0	3.5	381	414			0.32 - 24	221 - 629		23.5 - 420	0.2 - 21.9	136 - 503		
Y	32	9	24	9	0.5	0.8			3.3 - 153	0.23 - 2.13		0.14 - 17.7	1.6 - 373	0.1 - 0.4		
Zr	25	14	11	14	b.d.		400		1.2 - 158	b.d. - 5.6			0.7 - 156	0.02 - 0.53		
Nb	0.09	0.07	0.07	0.07	0.02	0.02			0.4 - 3.5	b.d. - 0.78			0 - 1.5	0.01 - 0.02		
Ba	0.05	0.03	0.06	0.03	38	112	230	210	0.6 - 40	13.4 - 103		4.47 - 464	0 - 57.1	9.4 - 56.9		
La	0.31	0.16	0.14	0.16	0.36	0.93	12.2	16.4	0.05 - 4.21	0.28 - 1.29		0.18 - 7.7	0 - 1.9	0.1 - 0.5	0.44 - 1.4	0.84
Ce	1.63	0.53	0.78	0.53	0.98	2.64	30	47	0.11 - 10.6	0.59 - 2.46		0.44 - 14.2	0 - 9.5	0.4 - 1.3	2.6 - 7.8	2.6
Pr	0.46	0.12	0.23	0.12	0.14	0.37			0.08 - 2.51	b.d. - 0.36			0 - 2.6	0.04 - 0.15		
Nd	3.64	0.90	1.83	0.90	0.70	1.64		45	0.29 - 18.1	b.d. - 1.43		0.22 - 18	0.1 - 22.2	0.2 - 0.7		
Sm	2.34	0.63	1.23	0.63	0.21	0.54	11.2	7.1	0.33 - 10.5	b.d.		0.04 - 5.8	0 - 15.4	0.1 - 0.2	0.99 - 5.1	0.59
Eu	0.21	0.06	0.08	0.06	3.09	5.35	1.2	1.8	0.09 - 0.56	1.29 - 4.52		0.40 - 3.3	0 - 1.0	0.8 - 3.4	0.10 - 0.45	5.34
Gd	4.38	1.35	2.78	1.35	0.19	0.27		1.4	0.42 - 18.1	b.d.		0.09 - 51	0.1 - 33.0	0.04 - 0.15		
Tb	0.81	0.22	0.51	0.22	0.04	0.06	3.3		0.10 - 3.69	b.d.			0 - 7.8	0.01 - 0.02	0.42 - 2.0	0.09
Dy	6.17	1.74	4.24	1.74	0.13	0.21	20		0.64 - 27.2	b.d.		0.03 - 2.6	0.2 - 58.5	0.02 - 0.10		
Ho	1.30	0.34	0.96	0.34	0.02	0.04	3.3		0.10 - 6.16	b.d. - 0.08			0.1 - 14.2	0.01 - 0.02		

Revision 2

Er	3.65 0.93	2.96 0.93	0.06 0.08			0.30 - 17.8	b.d. - 0.21		0.03 - 9.3	0.2 - 41.6	0.05		
Tm	0.53 0.16	0.46 0.16	0.02 0.01	4.6	1.3	0.08 - 2.83	b.d.						
Yb	3.55 0.78	3.27 0.78	0.08 0.09	11.2	5	0.44 - 21.2	b.d. - 0.25		0.03 - 2.5	0.2 - 40.5	0.07	2.4 - 7.2	0.27
Lu	0.47 0.14	0.49 0.14	0.012 0.004	1.65	0.56	0.09 - 3.27	b.d.			0 - 5.8	0.011 - 0.012	0.37 - 0.92	0.034
Hf	1.75 0.96	0.79 0.96	<i>b.d.</i>	5.5	5	0.18 - 8.26	b.d. - 0.21			0 - 6.4		0.58 - 1.2	0.15

757 Dashes indicate element not analyzed; b.d. = below detection limit.

758 Literature data from Hodges and Kushiro (1974); Papike et al. (1974, 1976); Dymek et al. (1975); Warner et al. (1975, 1976a, 1977); Haskin and Korotev (1977); Neal et al.  
 759 (1990); Schnare et al. (2008); Hui et al. (2011); Alexander et al. (2014); and Hallis et al. (2014).

760

761

762 Table 4. Results of fractionation calculations on 71597 composition.

	71597,1 <sup>a</sup>	Olivine	D <sub>OI/L</sub>	D <sub>ilm/L</sub>	olivine ( $\pm$ ilmenite) subtraction		
<i>wt %</i>					24% <i>ol</i>	27% <i>ol</i>	27% <i>ol</i> + 1% <i>ilm</i>
SiO <sub>2</sub>	39.2	37.9			39.61	39.68	40.44
TiO <sub>2</sub>	8.4	0.047			11.03	11.48	10.60
Al <sub>2</sub> O <sub>3</sub>	7.9				10.39	10.82	10.97
Cr <sub>2</sub> O <sub>3</sub>	0.47	0.22			0.55	0.56	0.56
FeO	19.8	24.3			18.49	18.26	17.84
MnO	0.237	0.26			0.23	0.23	0.23
MgO	15.8	37.1			8.96	7.79	8.03
CaO	7.9	0.26			10.31	10.72	10.87
Na <sub>2</sub> O	0.29				0.38	0.40	0.40
K <sub>2</sub> O	0.027				0.04	0.04	0.04
TOTAL	100	100.09			99.99	99.99	99.99
<i>ppm</i>							
Cr	3216	1854	0.92	10	3292	3303	2849
Co	43	64	3.5	2.2	21	19	19
La	3	[0.01]	0.011	0.029	3.9	4.1	4.2
Sm	3.9	[0.01]	0.0002	0.053	5.1	5.3	5.4
Eu	1	[0.01]	0.007	0.02	1.3	1.4	1.4
Yb	4.8	[0.01]	0.030	0.051	6.3	6.5	6.6
Hf	4.2	[0.01]	0.010	0.38	5.5	5.7	5.8
Cr/La	1072				836	806	686
La/Sm	0.77				0.77	0.77	0.77
Yb/Sm	1.23				1.22	1.22	1.22

763 <sup>a</sup>INAA Values reported in Murali et al. (1977). SiO<sub>2</sub> calculated to bring total to 100%.764 D<sub>OI/L</sub> values from equations of Bédard (2007), assuming initial bulk MgO was 9 wt%.765 D<sub>ilm/L</sub> values from Haskin and Korotev (1977) except Hf (Klemme et al. 2006).

766 Table 5. Mineral-melt partition coefficients used in modeling of 71597.

	olivine	armalcolite	ilmenite	plagioclase		augite		pigeonite	
V	0.49 <sup>a</sup>	6.7 <sup>c</sup>	3.4 <sup>c</sup>	0.010 <sup>h</sup>		1.1 <sup>k</sup>		0.33 <sup>a</sup>	
Cr	0.91 <sup>a</sup>	6.4 <sup>c</sup>	10 <sup>g</sup>	0.018	0.021 <sup>i</sup>	3.3 <sup>g</sup>		10 <sup>g</sup>	
La	0.011 <sup>a</sup>	0.006 <sup>d</sup>	0.029 <sup>g</sup>	0.013	0.022 <sup>j</sup>	0.05	0.14 <sup>l</sup>	0.004	0.023 <sup>l</sup>
Ce	0.008 <sup>a</sup>	0.007 <sup>d</sup>	0.035 <sup>g</sup>	0.015	0.022 <sup>j</sup>	0.08	0.18 <sup>l</sup>	0.006	0.035 <sup>l</sup>
Pr	0.006 <sup>b</sup>	0.007 <sup>d</sup>	0.041 <sup>g</sup>	0.037 <sup>g</sup>		0.12	0.22 <sup>l</sup>	0.01	0.052 <sup>l</sup>
Nd	0.005 <sup>a</sup>	0.008 <sup>d</sup>	0.047 <sup>g</sup>	0.012	0.018 <sup>j</sup>	0.2	0.30 <sup>l</sup>	0.021	0.098 <sup>l</sup>
Sm	0.0002 <sup>a</sup>	0.008 <sup>d</sup>	0.053 <sup>g</sup>	0.009	0.013 <sup>j</sup>	0.24	0.33 <sup>l</sup>	0.028	0.124 <sup>l</sup>
Eu	0.007 <sup>a</sup>	0.006 <sup>d</sup>	0.020 <sup>g</sup>	0.817	0.916 <sup>j</sup>	0.26	0.36 <sup>l</sup>	0.036	0.150 <sup>l</sup>
Gd	0.004 <sup>a</sup>	0.013 <sup>e</sup>	0.081 <sup>g</sup>	0.012 <sup>g</sup>		0.28	0.37 <sup>l</sup>	0.045	0.177 <sup>l</sup>
Tb	0.01 <sup>a</sup>	0.024 <sup>d</sup>	0.095 <sup>g</sup>	0.012 <sup>g</sup>		0.29	0.38 <sup>l</sup>	0.056	0.206 <sup>l</sup>
Dy	0.01 <sup>a</sup>	0.035 <sup>d</sup>	0.013 <sup>c</sup>	0.012 <sup>g</sup>		0.29	0.40 <sup>l</sup>	0.068	0.234 <sup>l</sup>
Ho	0.016 <sup>a</sup>	0.045 <sup>d</sup>	0.018 <sup>c</sup>	0.012 <sup>g</sup>		0.29	0.43 <sup>l</sup>	0.079	0.259 <sup>l</sup>
Er	0.023 <sup>a</sup>	0.056 <sup>d</sup>	0.024 <sup>c</sup>	0.001	0.004 <sup>j</sup>	0.29	0.46 <sup>l</sup>	0.09	0.280 <sup>l</sup>
Tm	0.026 <sup>b</sup>	0.060 <sup>f</sup>	0.331 <sup>g</sup>	0.012 <sup>g</sup>		0.28	0.47 <sup>l</sup>	0.1	0.297 <sup>l</sup>
Yb	0.030 <sup>a</sup>	0.070 <sup>d</sup>	0.051 <sup>c</sup>	0.012 <sup>g</sup>		0.27	0.49 <sup>l</sup>	0.109	0.310 <sup>l</sup>
Lu	0.053 <sup>a</sup>	0.070 <sup>e</sup>	0.067 <sup>c</sup>	0.011 <sup>g</sup>		0.26	0.49 <sup>l</sup>	0.117	0.321 <sup>l</sup>

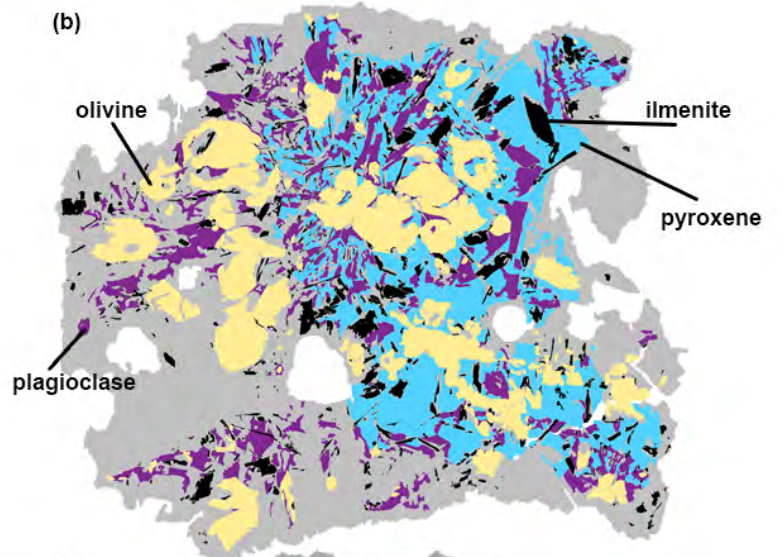
767 <sup>a</sup>Bédard (2005); <sup>b</sup>interpolated; <sup>c</sup>Dygert et al. (2013); <sup>d</sup>Neal et al. (1990); <sup>e</sup>Klemme et al.  
768 (2006); <sup>f</sup>Irving et al. (1978); <sup>g</sup>Haskin and Korotev (1977); <sup>h</sup>Bindeman et al. (1998); <sup>i</sup>RTlnD;  
769 <sup>j</sup>Hui et al. (2011); <sup>k</sup>Mallman and O'Neill (2009); <sup>l</sup>Sun and Liang (2012)

770

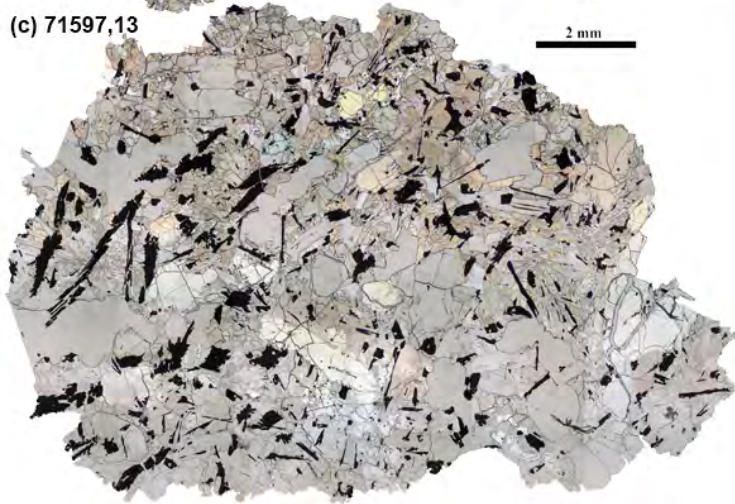
Figure 1  
(a) 71597,12



(b)



(c) 71597,13



(d)

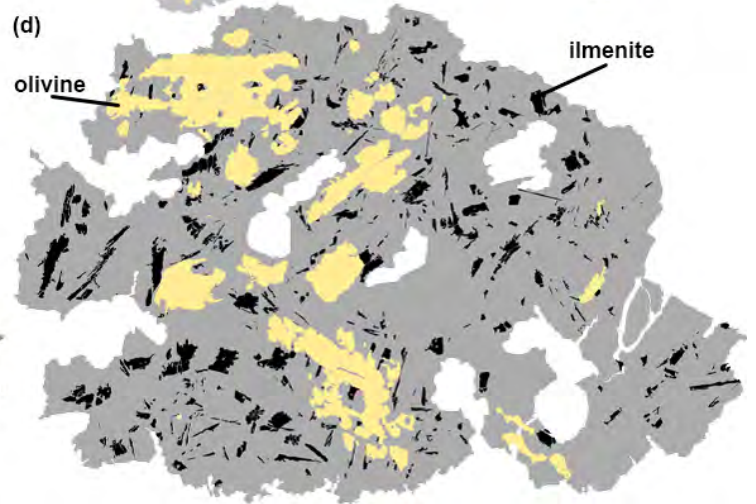




Fig. 2

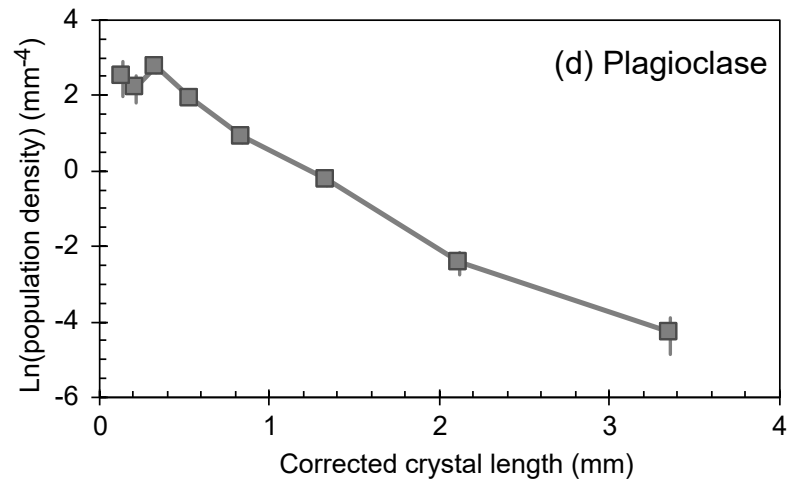
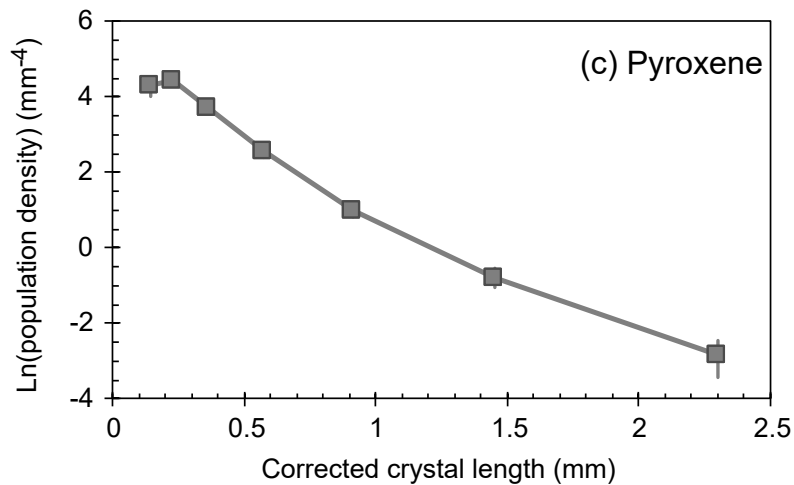
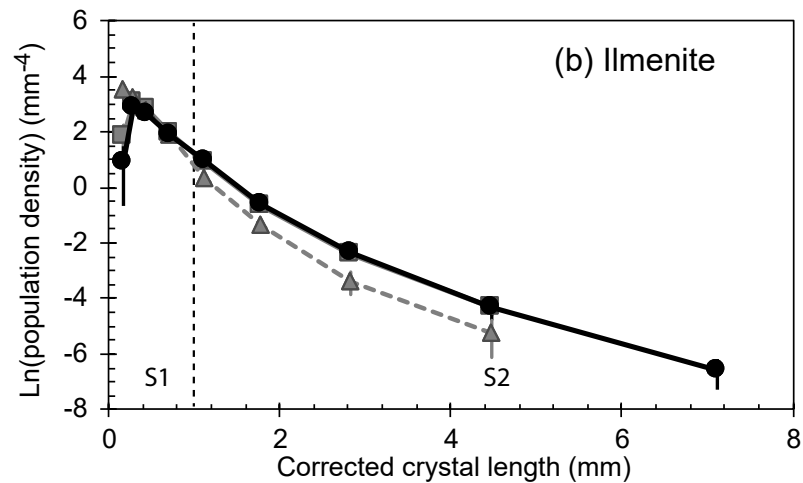
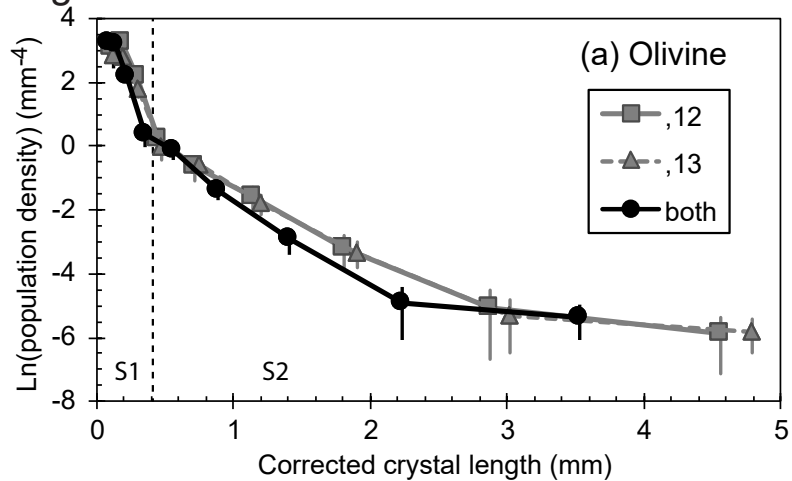




Fig. 4

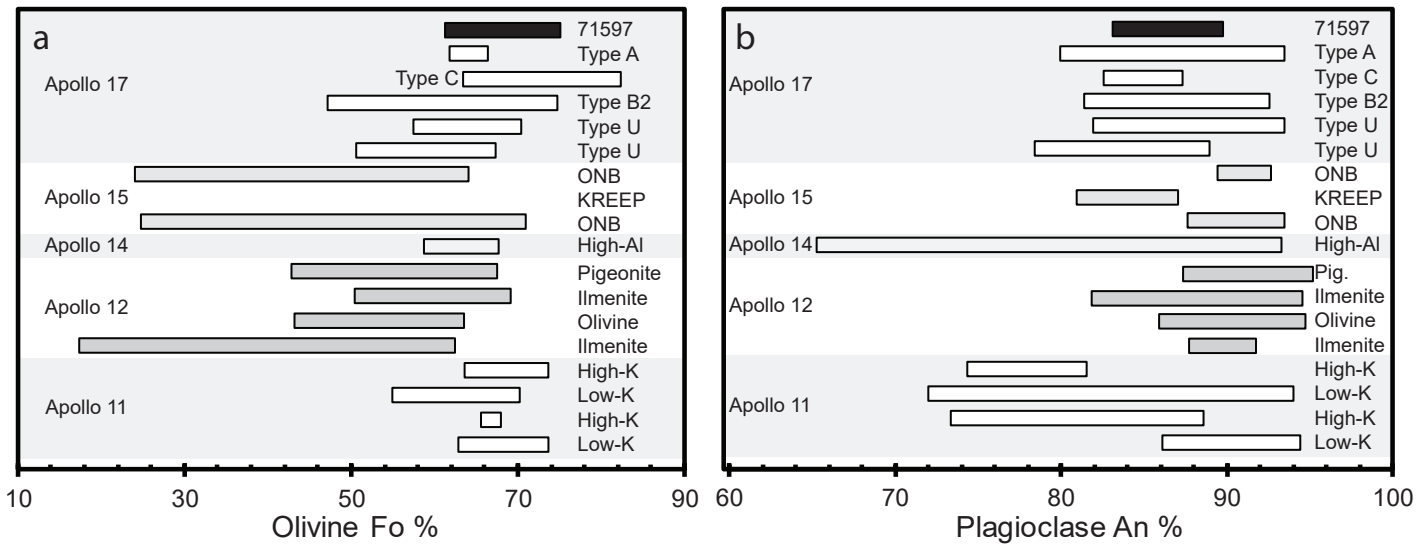


Fig. 5

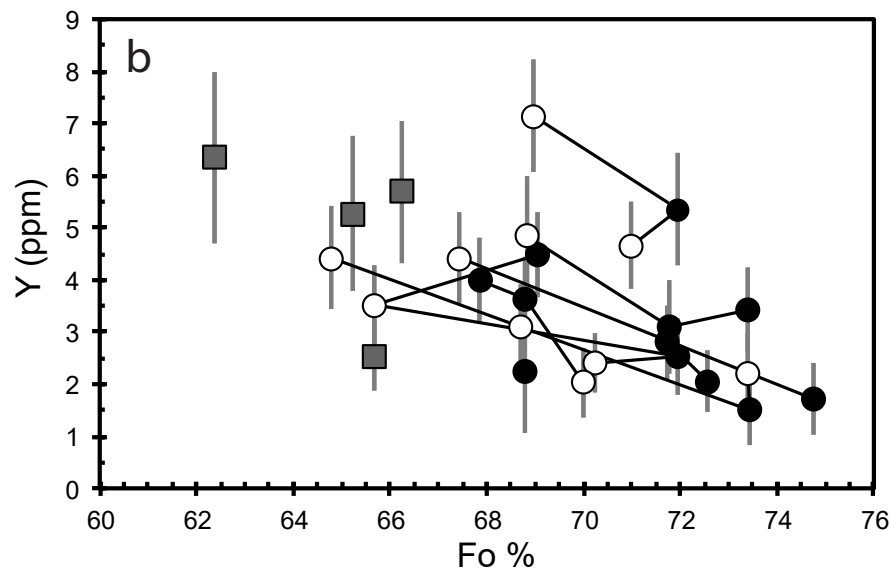
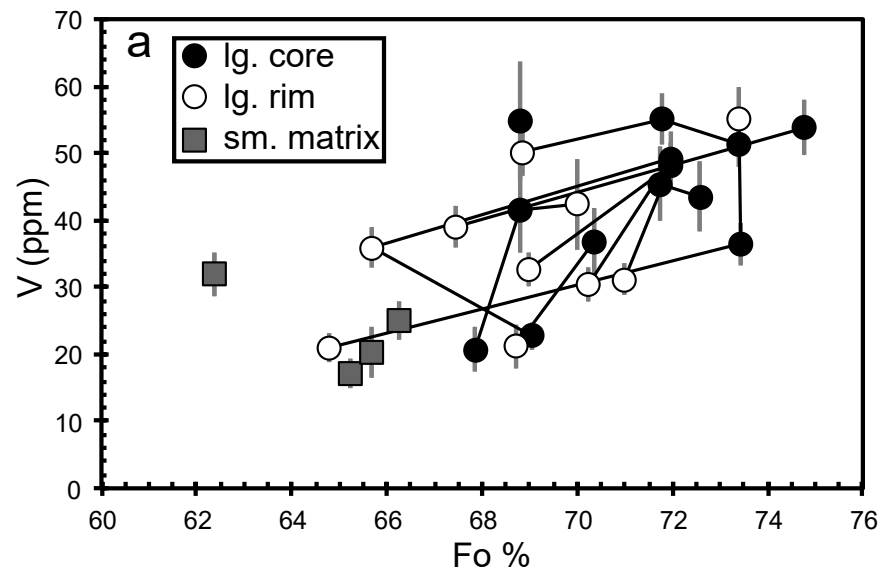


Fig. 6

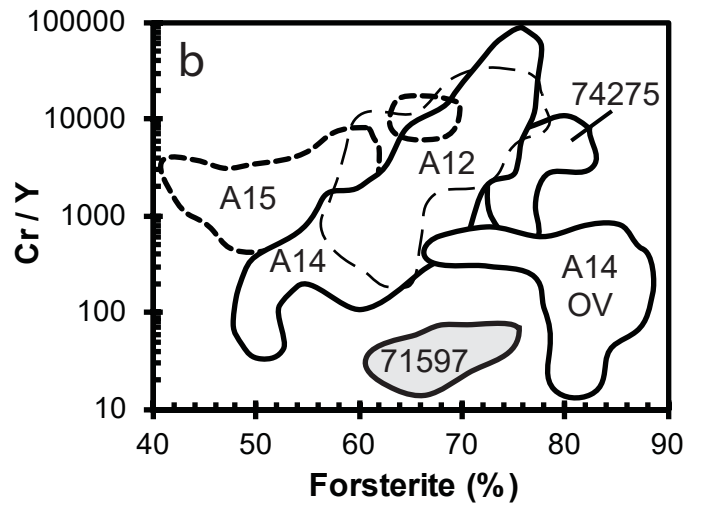
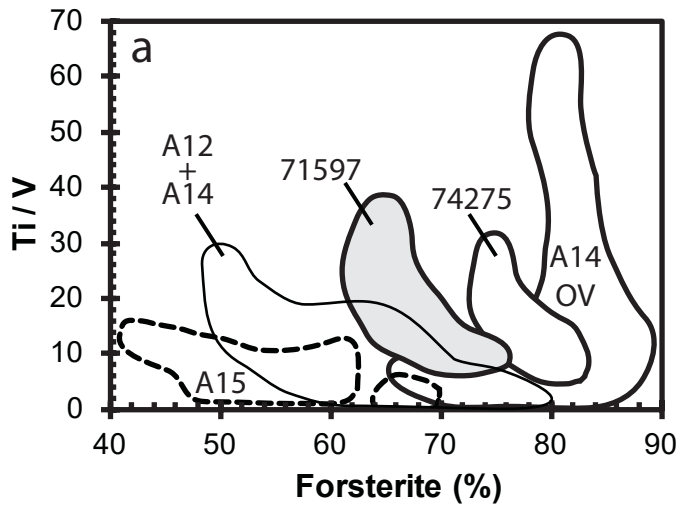


Fig. 7

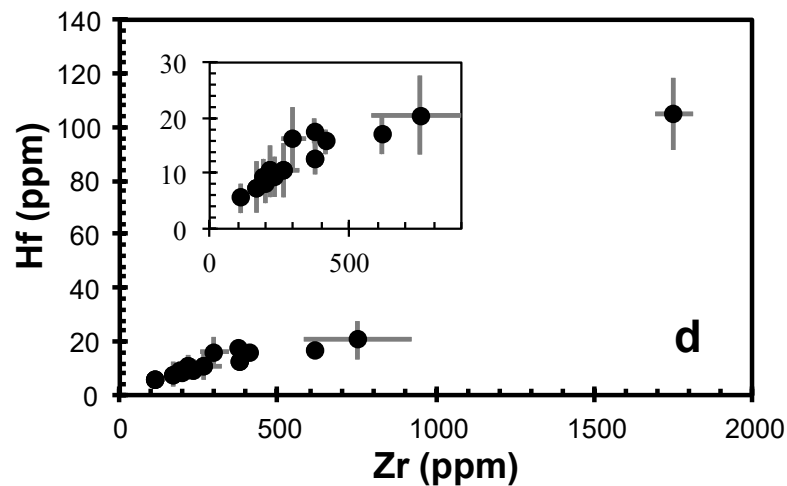
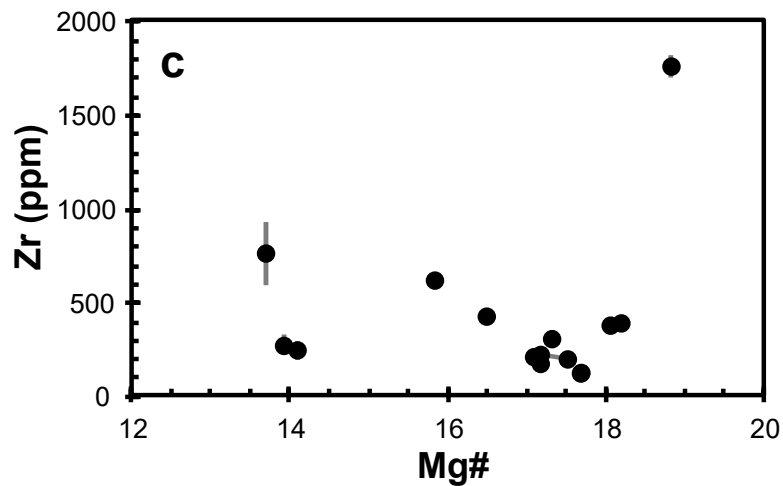
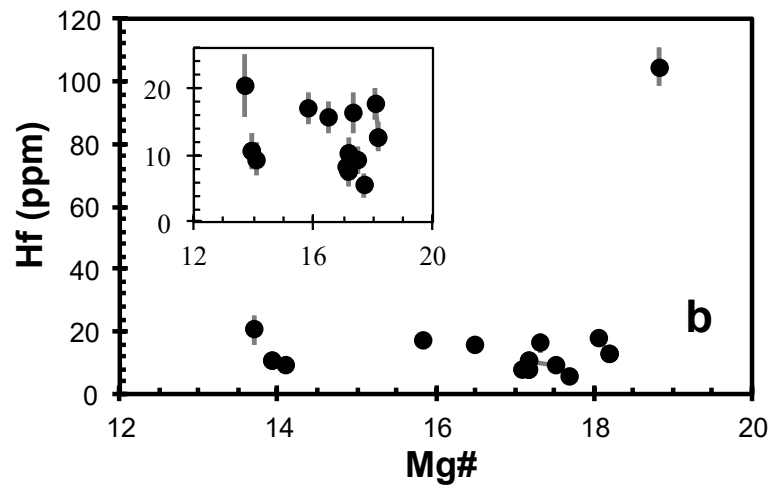
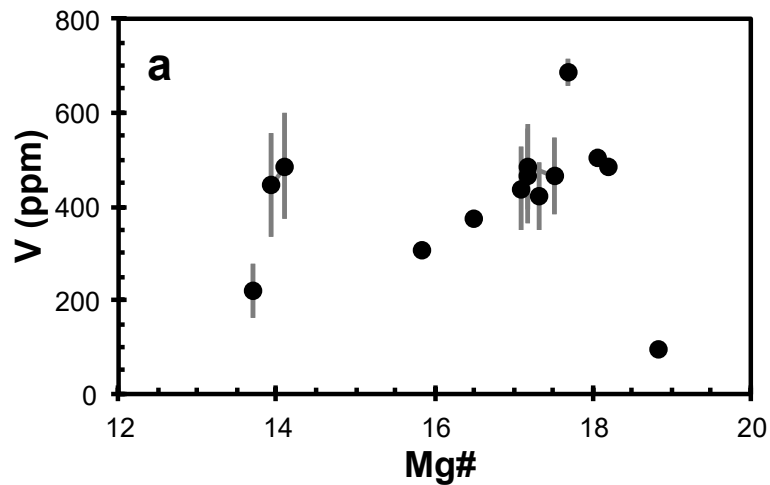
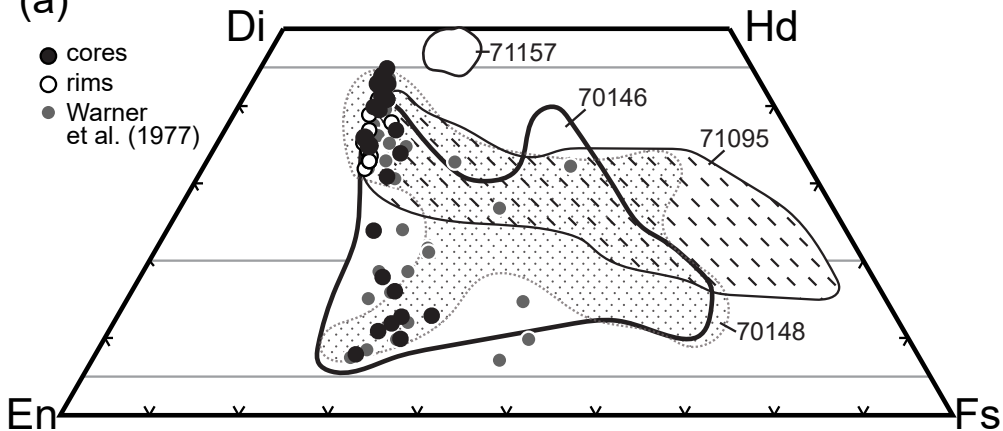


Fig. 8

(a)



(b)

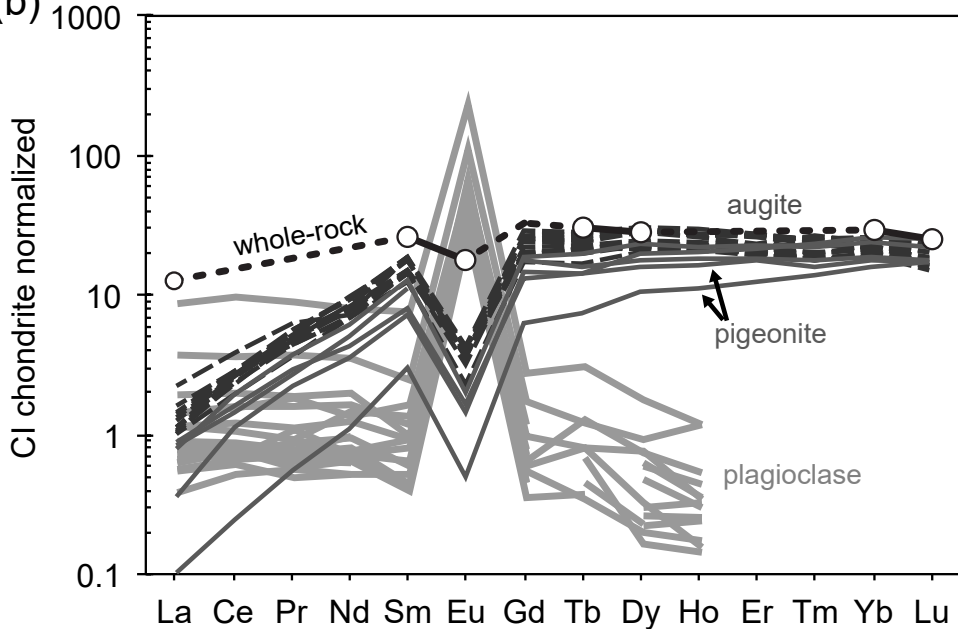


Fig. 9

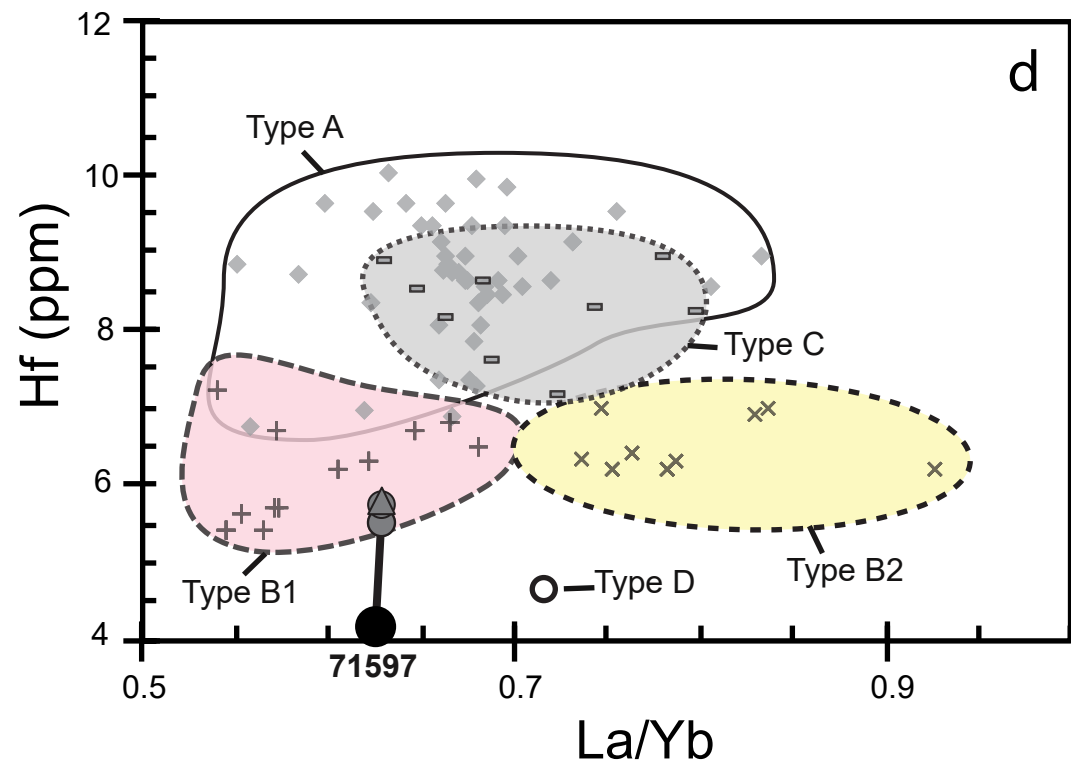
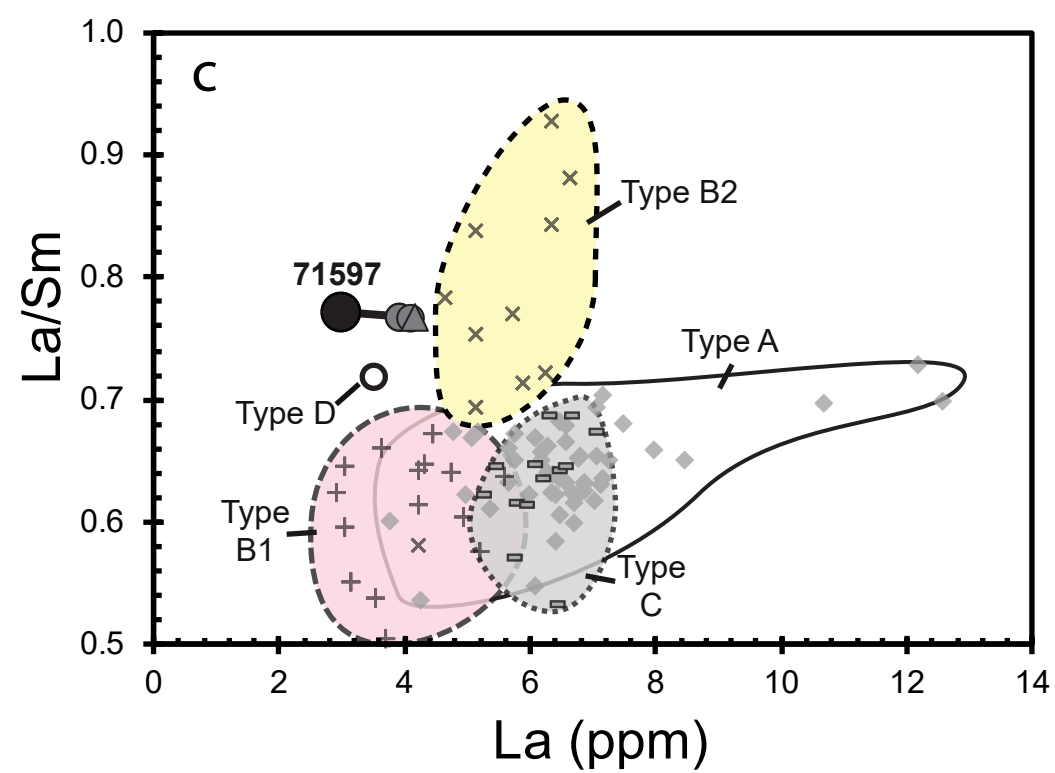
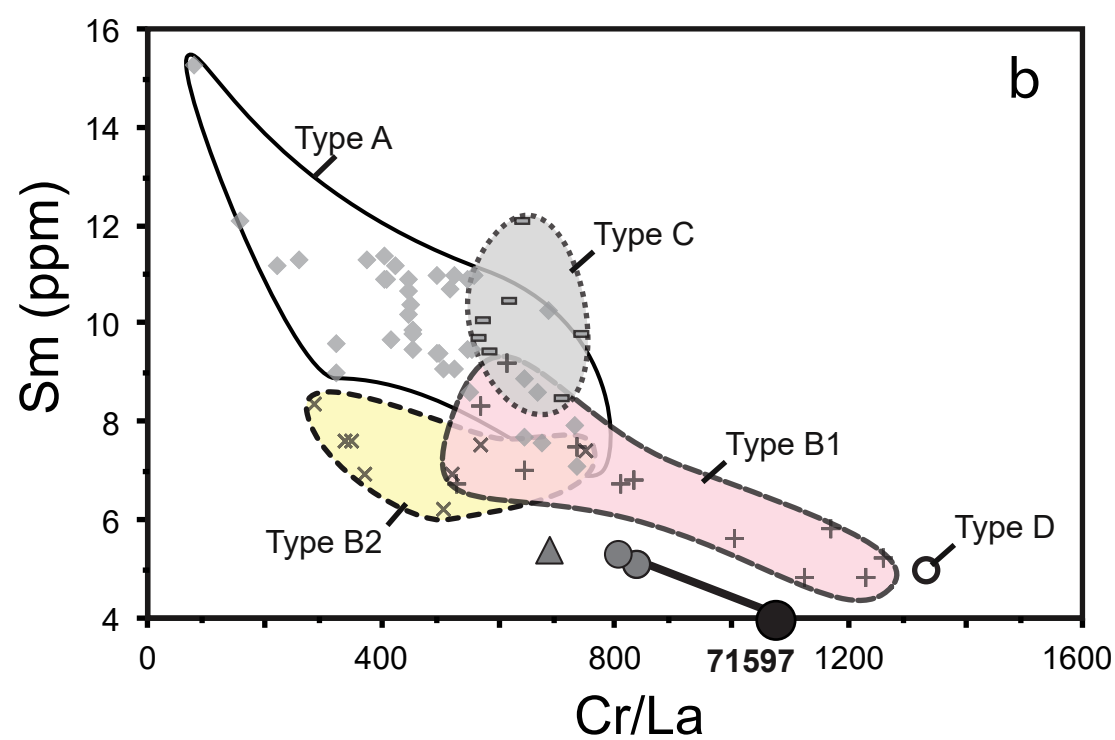
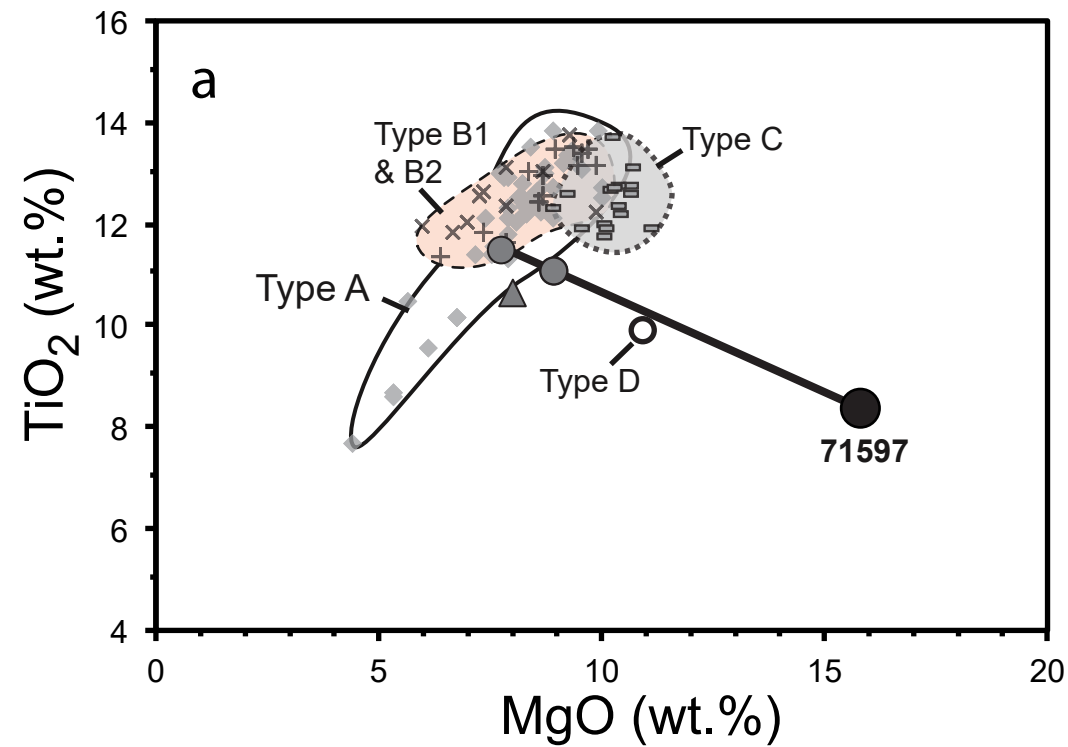




Fig. 10

